THESIS

COMPOSITIONAL TUNING, CRYSTAL GROWTH, AND MAGNETIC PROPERTIES OF

IRON PHOSPHATE OXIDE

Submitted by

Michael Tarne

Department of Chemistry

In partial fulfillment of the requirements

For the Degree of Master of Science

Colorado State University

Fort Collins, Colorado

Spring 2017

Master's Committee

    Advisor: James Neilson

    Matthew Shores
    Kate Ross

ABSTRACT

COMPOSITIONAL TUNING, CRYSTAL GROWTH, AND MAGNETIC PROPERTIES OF

IRON PHOSPHATE OXIDE

Iron phosphate oxide, $Fe_3PO_4O_3$, is a crystalline solid featuring magnetic Fe^{3+} ions on a complex lattice composed of closely-spaced triangles. Previous work from our research group on this compound has proposed a helical magnetic structure below $T = 163$ K attributed to $J_1 - J_2$ competing interactions between nearest-neighbor and next-nearest-neighbor iron atoms. This was based on neutron powder diffraction featuring unique broad, flat-topped magnetic reflections due to needle-like magnetic domains. In order to confirm the magnetic structure and origins of frustration, this thesis will expand upon the research focused on this compound.

The first chapter focuses on single crystal growth of $Fe_3PO_4O_3$. While neutron powder diffraction provides insight to the magnetic structure, powder and domain averaging obfuscate a conclusive structure for $Fe_3PO_4O_3$ and single crystal neutron scattering is necessary. Due to the incongruency of melting, single crystal growth has proven challenging. A number of techniques including flux growth, slow cooling, and optical floating zone growth were attempted and success has been achieved via heterogenous chemical vapor transport from $FePO_4$ using $ZrCl_4$ as a transport agent. These crystals are of sufficient size for single crystal measurements on modern neutron diffractometers.

Dilution of the magnetic sublattice in frustrated magnets can also provide insight into the nature of competing spin interactions. Dilution of the Fe^{3+} lattice in $Fe_3PO_4O_3$ is accomplished by substituting non-magnetic Ga^{3+} to form the solid solution series $Fe_{3-x}Ga_xPO_4O_3$ with $x = 0, 0.012, 0.06, 0.25, 0.5, 1.0, 1.5$. The magnetic susceptibility and neutron powder diffraction data of these compounds are presented. A dramatic decrease of the both the helical pitch length and the

domain size is observed with increasing x; for $x > 0.5$, the compounds lack long range magnetic order. The phases that do exhibit magnetic order show a decrease in helical pitch with increasing x as determined from the magnitude of the magnetic propagation vector. This trend can be qualitatively reproduced by increasing the ratio of J_2/J_1 in the Heisenberg model. Intriguingly, the domain size extracted from peak broadening of the magnetic reflections is nearly equal to the pitch length for each value of x, which suggests that the two qualities are linked in this unusual antiferromagnet.

The last chapter focuses on the oxyfluoride $Fe_3PO_{7-x}F_x$. Through fluorination using low-temperature *chimie douce* reactions with polytetrafluoroethylene, the magnetic properties show changes in the magnetic susceptibility, isothermal magnetization, and neutron powder diffraction. The magnetic susceptibility shows a peak near $T = 13$ K and a zero field cooled/field cooled splitting at $T = 78$ K. The broad, flat-topped magnetic reflections in the powder neutron diffraction exhibit a decrease in width and increase in intensity. The changes in the neutron powder diffraction suggest an increase in correlation length in the ab plane of the fluorinated compound.

Iron phosphate oxide is a unique lattice showing a rich magnetic phase diagram in both the gallium-substituted and fluorinated species. While mean-field interactions are sufficient to describe interactions in the solid solution series $Fe_{3-x}Ga_xPO_4O_3$, the additional magnetic transitions in $Fe_3PO_{7-x}F_x$ suggest a more complicated set of interactions.

ACKNOWLEDGEMENTS

My first thanks have to go to Jamie, who has been the best advisor one could imagine. Kate was also a great mentor and taught me so much about magnetism and neutrons. Everyone else in the Neilson group was (and is) great, and thank you for making grad school so awesome. Thanks to my family, who were perhaps more supportive than they should be. And last but definitely not least, Emily! Thanks for always believing in me and pushing me to be my best.

TABLE OF CONTENTS

1. Introduction and Background

1.1. Magnetism and Frustration

Magnetism in extended solids is intimately linked to the underlying crystal structure and the interaction between neighboring atoms and magnetic moments. Small perturbations such as doping can have macroscopic effects, especially in sensitive systems. Many of the systems with unpaired spins studied in solid state chemistry have an underlying magnetic order, such as ferromagnetism and antiferromagnetism, shown in Figure 1.1a and 1.1b. When more than one type of magnetic ordering is energetically favorable, interesting physical properties and complex magnetic states can form. These states of matter are complex, existing only because of the elaborate interactions at the microscopic level.

Geometric frustration is one way to induce exotic magnetic ordering in solids. Frustration often leads to the inability to find a unique ground state to satisfy all interactions within the system. One such example is shown in Figure 1.1. Square lattices can lead to ground states which satisfy antiferromagnetic (Figure 1.1b) ordering, but a simple triangular antiferromagnet (Figure 1.1c) does not allow all three spins to align antiparallel as an antiferromagnet would normally order and leads to six degenerate ground states. Triangular lattice motifs, including the 2D triangular lattice in the spinel structure, kagomé lattices, and the pyrochlore lattice, are common in frustrated systems and can lead to a variety of magnetic states, including noncollinear spin structures[1,2], spin glasses[3], multiferroics[4], and spin liquids[5].

Many of these emergent magnetic states have consequences in other areas of solid state chemistry or real-world applications. Quantum spin liquids are a magnetic analog of liquids in which the magnetic moments are disordered even at extremely low temperatures. These have been proposed
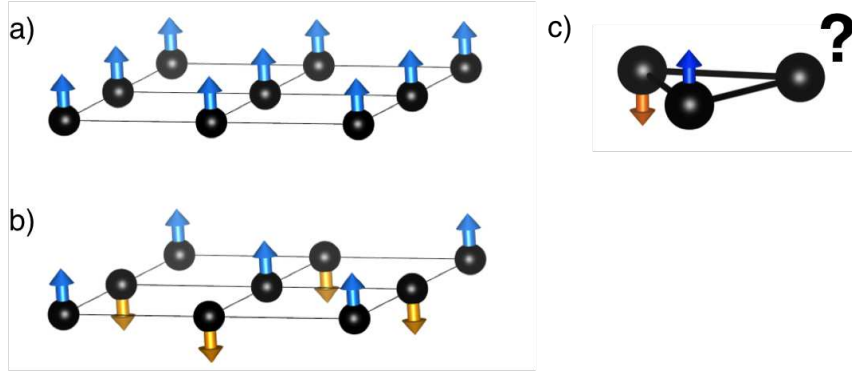
Figure 1.1: a) Ferromagnetic ordering on a square lattice. b) Antiferromagnetic ordering on a square lattice with nearest neighbors antiparallel. c) Triangular lattices with one-dimensional spins lead to geometric frustration and degenerate ground states.

for applications in quantum computing[6] or to study one proposed mechanism for high-temperature superconductivity[7]. A spin glass is a not-yet fully understood system in which frustration leads to a lack of magnetic long-range order, but a cooperative "freezing" transition occurs where the paramagnetic state freezes to a static but randomized spin glass state. Central to spin glasses are some sort of disorder or randomness, arising from interactions including random substition in the $Cu_{1-x}Mn_x$ alloys[8] or where the interaction strength is varied, such as in the spin glass $Rb_2Cu_{1-x}Co_xF_4$[9]. As with the spin liquids, the ground state is highly degenerate. Spin ices, like $Dy_2Ti_2O_7$, are interesting due to their similarities to water ice; the tetrahedral magnetic units follow the "two-in, two-out" structure of water ice with the same residual entropy $S = R/2\ln(3/2)$[10]. In addition, emergent quasiparticles resembling magnetic monopoles have been found in $Dy_2Ti_2O_7$[11]. These complex magnetic states show the interesting way microscopic properties can converge to display unusual macroscopic phenomena.

In addition to geometric frustration, another source of frustration in magnetic solids is competing interactions. Even without geometric frustration, antiferromagnetic interactions between nearest-neighbors (NN) and next-nearest-neighbors (NNN) do not allow for magnetic ordering to satisfy both sets of antiferromagnetic interactions; these are referred to as J_1 and J_2 interactions
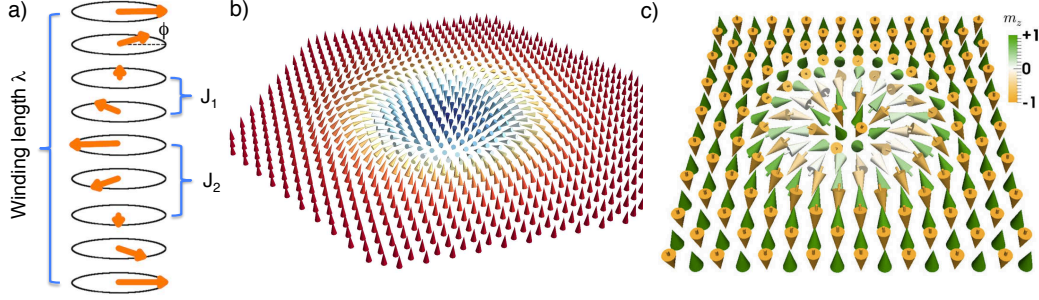
Figure 1.2: a) Helimagnet caused by J_1/J_2 interactions. The J_1 nearest-neighbor and J_2 next nearest neighbor interactions are shown, as well as the angle between neighboring spins, ϕ . b) Neél type Skyrmion, taken from dos Santos Dias, Bouaziz, Bouhassoune, Blügel, Lounis[12] and used under a CC-BY-4.0 license. d) Antiferromagnetic Skyrmions can be described as a superposition of two Skyrmions of opposite direction. Figure from Zhang, Zhou, and Ezawa[13] and used under a CC-BY-4.0 license.

as in the exchange integral that characterizes the interaction strength as shown in Equation 1.1.

$$\hat{H} = -J_1 \sum_{\langle i,j \rangle} \mathbf{S}_i \cdot \mathbf{S}_j - J_2 \sum_{\langle\langle i,k \rangle\rangle} \mathbf{S}_i \cdot \mathbf{S}_k \tag{1.1}$$

In this equation, J_1 and J_2 are the exchange interactions, $\mathbf{S}_i, \mathbf{S}_j$ are the spins on nearest-neighbor atoms, and $\mathbf{S}_i, \mathbf{S}_k$ represent next-nearest-neighbor interactions. One common magnetic ground state for $J_1 - J_2$ frustrated systems is magnetic helices, shown in Figure 1.2a. The period of the helix is determined by the relative strengths of the interaction parameters.

The underlying crystal chemistry can play a major role in the magnetic ordering of extended solids. For example, non-centrosymmetric unit cells can have additional magnetic interactions due to their asymmetry. One commonly studied system of non-centrosymmetric magnetic materials is the B20 compounds whose members include MnSi, $Fe_{1-x}Co_xSi$, and Cu_2OSeO_3. In non-centrosymmetric unit cells, competing interactions can arise from the underlying magnetic order and the Dzyaloshinsky-Moriya (DM) interaction, in which spin-orbit coupling mediates the interaction between the magnetic ground state of one atom and the excited state of one of its neighbors[14]. The DM interaction can be described by the Hamiltonian in Equation 1.2[14].
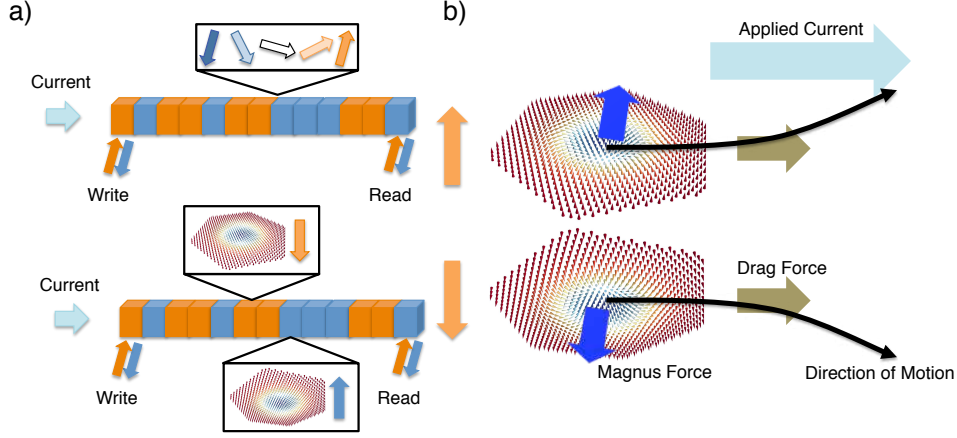
Figure 1.3: Racetrack memory architecture. a) Domain-wall based racetrack memory, where domains store binary information. b) Skyrmion-based spintronic material, where the polarization of the Skyrmion is the storage mechanism. Figures a and b adapted from Krause and Wiesendanger [17]. c) Antiferromagnetic Skyrmions; the Magnus force moves ferromagnetic Skyrmions perpendicular to the applied current along the black arrow. As the antiferromagnetic Skyrmion is a superposition of the two, the Magnus force cancels and the Skyrmion moves in the direction of the applied current. Figure adapted from Barker and Tretiakov [16].

$$\hat{H}_{DM} = \mathbf{D} \cdot \mathbf{S}_1 \times \mathbf{S}_2 \qquad (1.2)$$

The vector $\mathbf{D}$ goes to zero with inversion symmetry in the bond between the interacting atoms. When $\mathbf{D}$ is non-zero, the interaction energy is minimized at a $90°$ angle to the $\mathbf{D}$ vector between J_1 and J_2. In physical systems, the DM interaction is much weaker than ferromagnetism or antiferromagnetism, leading to canting of spins in the system and extended magnetic defects like Skyrmions.

Magnetic Skyrmions are a newly-discovered emergent phenomenon which can be described as chiral vortex-like spin textures and are shown in Figure 1.2b. The "Skyrmion lattice" is a hexagonal close-packed lattice of layered Skyrmions. Skyrmions have potential applications in magnetic storage, as their chiral nature (the rotational direction of the "vortex") is a natural way to store the binary information computer architecture currently utilizes. Magnetic racetrack storage is a one-dimensional storage method depicted in Figure 1.3a, in which an "up" or "down" bit is written with a magnetic field and moved by applying a current pulse. These bits can be read by

either a separate read head, as shown in the figure, or by applying a current pulse with opposite bias to move the bits backwards to read at the same point where they are written. Theoretically, racetrack storage would allow for more compact magnetic storage devices with faster read/write times and lower power consumption than current technology affords[15]. Two strong candidates for this application are domain-wall-based storage, in which magnetic domains and the resultant domain walls store information, or Skyrmions. Domain walls have the disadvantage of pinning by defects which means trying to move them in racetrack storage architectures requires a high current, resulting in Joule heating. Skyrmions are able to move past lattice point defects due to their mesoscopic scales, and so the devices require lower current. Skyrmions also have a non-zero topological charge, so they cannot be continuously distorted back to a simple magnetic order. The only way to destroy a Skyrmion is by moving the swirl off of the edge of the material so information loss is minimized as compared to domain wall architecture. All materials with Skyrmion lattices thus far have the downside of being based on ferromagnetic materials, making them susceptible to stray magnetic fields. They also have a net magnetization, so when a current is applied to move Skyrmions through the material, they experience a Magnus force proportional to $\hat{n} \times \mathbf{j}$, where $\hat{n}$ is the direction of the magnetization in the center of the Skyrmion and $\mathbf{j}$ is the direction of the applied current. This Magnus force serves to move the Skyrmion longitudinally relative to the applied field and likely off the edge of the storage architecture. One solution to this issue is the use of antiferromagnetic Skyrmionic materials. Theoretical work shows that antiferromagnetic Skyrmions can be thought of as superimposed lattices of ferromagnetic Skyrmions, shown in Figure 1.2c. As a result, the Magnus force cancels and the antiferromagnetic Skyrmion moves in the direction of the applied current[16]. Antiferromagnetic materials are also much more common in nature. However, Skyrmions have not been discovered in any material with net antiferromagnetic interactions, so these advantages are still purely theoretical.

1.2. Magnetic Wavevector Notation

In extended solids, it is common for spins to point in directions other than "up" and "down," as is the convention in much of chemistry. As such the magnetic propagation vector $\mathbf{k}$ is used. This vector quantity describes the magnetic structure in reciprocal space with respect to the underlying nuclear lattice. The moment $\mathbf{m}_j$ is written in the form found in Equation 1.3[18]:

$$\mathbf{m}_j = \Psi_j^k e^{-2\pi i \mathbf{k} \cdot \mathbf{t}} \tag{1.3}$$

Where Ψ_j^k is a magnetic basis vector and $\mathbf{t}$ is a lattice translation. For example, in the two-dimensional ferromagnetic lattice pictured in Figure 1a, $\mathbf{k} = (0\,0)$. When using the basis vector $\Psi_j = (0\,0\,1)$, moving from one lattice point to the next (a translation of $(0\,1)$) corresponds to:

$$\mathbf{m}_j = (0\,0\,1)e^{-2\pi i(0\,0)\cdot(0\,1)} = (0\,0\,1)e^0 = (0\,0\,1)$$

Leaving the moment unchanged. For the antiferromagnetic lattice in Figure 1b, $\Psi_j = (0\,0\,1)$ again, but $\mathbf{k} = (\frac{1}{2}\frac{1}{2})$. Upon the same translation:

$$\mathbf{m}_j = (0\,0\,1)e^{-2\pi i(0\,1)\cdot(\frac{1}{2}\frac{1}{2})} = (0\,0\,1)e^{-\pi i} = (0\,0\,\overline{1})$$

Which reverses the sign upon the lattice transition to the nearest lattice point[18]. One more translation, corresponding to $\mathbf{t} = (0\,0\,2)$, is applied:

$$\mathbf{m}_j = (0\,0\,1)e^{-2\pi i(0\,2)\cdot(\frac{1}{2}\frac{1}{2})} = (0\,0\,1)e^{-2\pi i} = (0\,0\,1)$$

And the spin returns to its original orientation. It is also possible to denote the aforementioned incommensurate structures with this notation. For example, the wavevector $\mathbf{k} = (0.243\,0\,0)$ would be incommensurate along the $\mathbf{k}_x$ direction (with a periodicity of $2\pi/\mathbf{k}$ unit cells) and commensurate along the $\mathbf{k}_y$ and $\mathbf{k}_z$ directions. This incommensurate structure would be a "sine" structure in which the amplitude of the magnetic moment is modulated. Helical magnetic structures are described by the following equation[18]:

$$\mathbf{m}_j = 2\text{Re}(\Psi_j^k)[\cos(-2\pi\mathbf{k}\cdot\mathbf{t}) + sin(-2\pi\mathbf{k}\cdot\mathbf{t})] \tag{1.4}$$

1.3.   Instrumental Methods and Techniques

A variety of instrumental methods are required to characterize extended solids and the resultant magnetic properties. The first major technique is X-ray diffraction, both single crystal (SCXRD) and powder (PXRD). X-ray diffraction relies on the elastic scattering of incoming radiation by the electron clouds of atoms. Constructive interference produces characteristic reflections when Equation 1.5 is satisfied:

$$2\mathbf{k}\cdot\mathbf{G} + G^2 = 0, \tag{1.5}$$

where $\mathbf{G}$ is any reciprocal lattice vector. The spacing $d(hkl)$ between lattice planes can be rewritten as $2\pi/|\mathbf{G}|$ and the magnitude of $\mathbf{k}$ is equivalent to $2\pi/\lambda$ where λ is the wavelength of the incident radiation. Thus the diffraction condition can be rewritten as:

$$2d\sin\theta = n\lambda \tag{1.6}$$

Which is of the form derived by Bragg[19]. As the X-rays are scattered by the electron cloud, scattering intensity and the structure factor are proportional to the atomic number. Powder X-

ray diffraction relies on the same principle, but the polycrystalline powder scatters equally in all directions which results in powder averaging and rings of diffraction.

Neutron scattering is a complimentary technique to X-ray diffraction in condensed matter. The neutron is a neutral $S = \frac{1}{2}$ particle, diffracting off of the nucleus *via* the strong nuclear force instead of the electron cloud. One consequence of this is that the structure factor and scattering intensity no longer follow monotonically with the atomic number, such that light elements can be studied when near heavy elements, such as in the compound WO_3, where the oxygen atoms can be hard to detect as X-ray scattering from tungsten is roughly 86 times stronger than that from oxygen atoms. In contrast, the coherent scattering cross sections are 2.97 barn for W and 4.232 barn for O, resulting in similar scattering from each[20]. Neutron scattering can also be used to characterize magnetic order in solids, as the neutron has a magnetic moment that can interact with ordered moments in the solid. Above the magnetic ordering temperature, only coherent scattering from the nuclear lattice is present. Cooling below T_N or T_C results in additional reflections from magnetic structures. The data in this thesis makes use of neutron powder diffraction (NPD) on polycrystalline powder samples. Single crystal neutron scattering is also possible, removing the effect of powder averaging and making refinement of the magnetic structure simpler. Neutron scattering has the significant downside that neutrons are difficult to produce with the flux required for scattering measurements; the primary ways to produce neutrons for such experiments are nuclear reactors or by striking heavy elements with the beam from a particle accelerator, spalling off neutrons. In contrast, X-ray diffraction is commonly done in research laboratories.

Physical properties measurements of the magnetization, magnetic susceptibility, and heat capacity are also crucial to characterizing magnetic materials. One instrument used for both of these is the Physical Properties Measurement System (PPMS), produced by Quantum Design, Inc. Magnetic susceptibility and magnetization is measured using a vibrating sample magnetometer (VSM),

in which the sample is oscillated at 40 Hz by a linear motor through a pair of pickup coils. The induced current in the coils is proportional to the magnetic moment. The PPMS allows VSM measurements down to 1.8 K and at magnetic fields up to 14 T. Heat capacity measurements are also performed on the PPMS; the instrument thermally isolates the sample and mounting platform and calculates the heat capacity via the quasi-adiabatic heat pulse method. This relies on applying a known power pulse to raise the temperature of the sample and measuring the relaxation time. An addendum is measured first using only the stage and mounting grease; this is the background and is automatically calculated and subtracted from the data by the PPMS software. The heat capacity option can also be utilized with the dilution refrigerator, which relies on the heat of mixing of ^{3}He/^{4}He for temperature control down to 50 mK[21]. These ultralow temperatures are often required to characterize magnetic transitions in highly frustrated materials.

1.4.   Iron Phosphate Oxide, $Fe_3PO_4O_3$

Much of this research focuses on the compound $Fe_3PO_4O_3$, iron phosphate oxide. The structure of $Fe_3PO_4O_3$ can be described as triangular units of distorted FeO_5 trigonal bipyramids coordinated by phosphate groups as shown in Figure 1.4a. Figures 1.4b and c shows the connectivity of magnetic Fe^{3+} cations; J_1 nearest-neighbor interactions are shown in blue within the triangles and J_2 next-nearest-neighbor interactions are shown in orange between neighboring triangles. When these interactions are both antiferromagnetic and Heisenberg-like (justified based on the lack of single-ion anisotropy expected for $S = \frac{5}{2}$ Fe^{3+} and significant direct exchange interactions[22]), this model produces helical magnetic states near the frustrated point $J_2/J_1 \approx 2$. J_2 is likely larger than J_1 due to the angular dependence of the superexchange interaction, $i.e.$ that the Fe$-$O$-$Fe bond is closer to 180°for the next-nearest-neighbor for the inter-triangular interaction[23]. As shown in previous work, the frustration is also likely to be responsible for the development of nearly vertical domain walls (i.e., needle-like domains)[24].
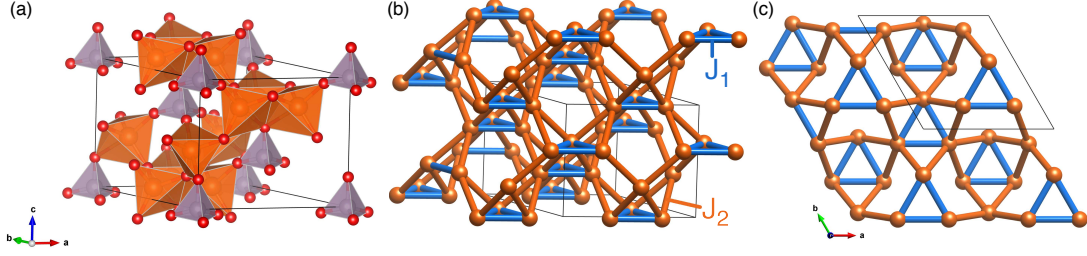
Figure 1.4: a) Crystal structure of $Fe_3PO_4O_3$. Iron is shown in orange, phosphorus in purple, and oxygen in red. b) Fe-Fe magnetic interactions in $Fe_3PO_4O_3$. J_1 bonds are highlighted in blue, J_2 bonds are shown in orange. c) View along the c axis of the magnetic interactions within $Fe_3PO_4O_3$ to highlight the planar nature of the J_1 interactions.

$Fe_3PO_4O_3$ has been previously studied via several characterization methods including magnetization [22,25], specific heat [26], Mössbauer spectroscopy [22,25], and neutron powder diffraction [22]. Previous work from the research group reported magnetization measurements on $Fe_3PO_4O_3$ and the magnetically diluted series $Fe_{3-x}Ga_xPO_4O_3$ and obtained accurate estimates of the mean-field Curie-Weiss interaction strength, θ_{CW}, which ranges from $\theta_{CW} < -1000$ K for $Fe_3PO_4O_3$ to –300 K for $Fe_{0.5}Ga_{2.5}PO_4O_3$ [24]. These large negative values imply strong antiferromagnetic interactions, even in the presence of significant magnetic dilutions. Curie-Weiss analysis, fitting a linear region of χ^{-1} using Equation 1.7:

$$\chi = \frac{C}{T - \theta_{CW}} \tag{1.7}$$

In this equation, C is the Curie constant and θ_{CW} is the Weiss constant, a measure of the magnetic interaction strength within the mean field model. The effective paramagnetic moment, p_{eff}, can be extracted from the fit as well: $p_{eff} = \sqrt{8C}$. The analysis shows very strong magnetic interactions; the Curie-Weiss analysis cannot be performed until significant dilution of the mean field interactions with gallium substitution ($Fe_{1.5}Ga_{1.5}PO_4O_3$).

The compound is assumed to be high-spin Fe^{3+} in a trigonal bipyramidal crystal field so the expected p_{eff} for this $S = \frac{5}{2}$ compound is 5.91. The measured value from Curie-Weiss analysis is significantly lower, trending towards $p_{\text{eff}} = 5.1$ at higher x values. This reduced moment is likely not due to a reduced Landé g value in the half-filled Fe^{3+} ion, but is instead caused by covalency or

ligand charge transfer. Partial charge transfer from the oxygen would serve to reduce the number of unpaired spins on the Fe. This reduction of the moment is consistent with the literature; a similar effect has been found in $\alpha-Fe_2O_3$[27] and $Ca_3Fe_2Ga_3O_{12}$[28]. A value of $p_{\text{eff}} = 5.1$ would lead to $S = 2.1$ or a value of $\mu = 4.2\mu_B$, which is also consistent with the refined moment from the neutron diffraction.

$Fe_3PO_4O_3$ (noncentrosymmetric space group, $R3m$) forms an antiferromagnetic helical magnetic state below $T_N = 163$ K determined by heat capacity and magnetic susceptibility measurements. The correlation length of the magnetic order extends to at least 90 nm along the c axis (in the hexagonal setting of $R3m$), but remains limited to $\xi_{ab} \sim 7$ nm in the ab plane down to at least $T = 4$ K[24], implying a high density of helical domain walls. This can be seen in the broadening required to fit the broad, flat-topped peaks seen below T_N in the NPD. The formation of the incommensurate helical state in $Fe_3PO_4O_3$ and its needle-like magnetic domains has been discussed in terms of frustration between antiferromagnetic nearest neighbor (J_1) and next nearest neighbor (J_2) interactions[24].

1.5. Motivation and Organization

While a preliminary magnetic structure for $Fe_3PO_4O_3$ has been determined, a number of questions still exist. The first is a confirmation of the magnetic structure described in Section 1.4 through single-crystal magnetic neutron diffraction. The process of single crystal growth, including a possible mechanism by which the chemical vapor transport reaction occurs, is described in Chapter 2. Chapter 3 describes the non-magnetic dilution of the compound through gallium substitution on the iron sites to form the solid solution series $Fe_{3-x}Ga_xPO_4O_3$. The modification of the magnetic interactions within the material lend insight into how the $J_1 - J_2$ competing interactions can affect the helical structure within iron phosphate oxide. The unique domains seen in the parent compound are also re-evaluated with additional data extracted from neutron powder diffraction re-

finements. The last chapter focuses on fluorine-doped $Fe_3PO_4O_3$, including magnetic susceptibility measurements and neutron powder diffraction. These three experiments will lend insight into how the magnetic frustration and interactions in $Fe_3PO_4O_3$ lead to the magnetic structure seen in the compound.

2. Crystal Growth of $Fe_3PO_4O_3$

2.1. Introduction and Initial Attempts

The introduction discussed the proposed magnetic structure for $Fe_3PO_4O_3$ based on powder neutron diffraction at low temperature. One major unresolved issue is whether the magnetic structure has one ordering wavevector (a single-$\mathbf{k}$ structure) with broadening as published[24] or contains several in a multi-$\mathbf{k}$ structure. As these peaks would be located at approximately the same value of Q, they would overlap in a way similar to the broad, flat-topped magnetic reflections seen in the neutron powder diffraction pattern of $Fe_3PO_4O_3$. Single crystals of the compound are required to discern the full magnetic structure.

To date, crystal growths by the author have been attempted with flux growth, slow cooling from a melt, vapor transport, and optical floating zone technique (OFZ). One issue that makes crystal growth of this material difficult is that it melts incongruently. On the $Fe_3(PO_3)_3$-Fe_2O_3 phase diagram, $Fe_3PO_4O_3$, found at 75mol% Fe_2O_3, decomposes at 1090 °C to liquid $FePO_4$ and solid Fe_2O_3[29]. In addition to the incongruent melting, ferric phosphates tend to reduce when heated to high temperatures in air. A sample of $Fe_3PO_4O_3$ heated to 1150 °C in air and quenched showed no $Fe_3PO_4O_3$ but instead a mixture of $FePO_4$, Fe_2O_3, and $Fe_2P_2O_7$, ferrous pyrophosphate[29]. The phase diagram[29] is consistent with the attempted crystal growths by slow cooling and OFZ technique. Slow cooling from a melt was attempted by preparing a peritectic mixture of 59 mol% Fe_2O_3 and 41 mol% $FePO_4$. The peritectic is the intersection of the $Fe_3PO_4O_3$ decomposition line with the liquidus surface; a eutectic mixture slightly enriched with Fe_2O_3 was used in an attempt to grow $Fe_3PO_4O_3$ crystals in a flux of molten $FePO_4$. The mixture was homogenized by manual grinding and placed in a Bridgman crucible in a vertical furnace, with the crucible positioned so the

13

top of the material was level with the thermocouple in the furnace, creating a small temperature gradient within the crucible to facilitate mixing and aid crystal growth in the cooler portion of the melt located at the tip of the crucible. The crucible and $FePO_4$-Fe_2O_3 mixture was heated to 1100 °C for 36 h to ensure the mixture was fully melted, following by cooling at 0.5°C/hr to 950 °C and then cooling at 100 °C/hr to room temperature. Visually, the ingot seemed to contain a great number of tiny crystals (too small to handle with tweezers) and a brown powder. X-ray diffraction of the pulverized ingot contains a mixture of $FePO_4$ and $Fe_3PO_4O_3$, as would be expected; however, the crystals obtained from this method are too small for further analysis. Slower cooling could be one method to improve the crystals grown by slow cooling; however, 0.5 °C/hr is already a very slow rate. Vibration isolation could also improve the results, as the critical nuclei are likely sensitive at formation. However, this method will probably produce similar results to chemical vapor transport, which has already been successful.

The optical floating zone technique relies on using light (usually from xenon or halogen lamps) and mirrors to melt a feed rod and seed rod of polycrystalline material to create a molten "floating zone." Two rods of sintered $Fe_3PO_4O_3$, the feed and seed rods, are melted together to form the "zone." The melted rods are counter-rotated to increase convection and the rods are moved to move the zone and attempt to grow a crystal. The goal is that one crystalline domain will dominate the growth and begin to grow a large single crystal; these will be approximately 8 mm in diameter and can be several centimeters long. To date, we have attempted two crystal growth techniques with the optical floating zone technique, one using the traveling solvent OFZ technique and one using pure $Fe_3PO_4O_3$. The traveling solvent method uses a different composition at the end of the seed rod (the eutectic composition) to create a stable zone of the desired product before adding more of the feed rod. In the attempt with just $Fe_3PO_4O_3$, the zone never stabilized; instead, something offgassed and the iron phosphate oxide decomposed. By PXRD, the zone contained Fe_2O_3, $Fe_7(PO_4)_6$, and

$Fe_3(PO_4)_2$ after cooling. The presence of ferrous oxides/phosphates suggests decomposition of $FePO_4$ and too high of a temperature in the zone. Use of lower power lamps (600 W instead of 1500 W) gives more control over temperature in the range at which the growth would occur. Use of these lamps combined with the traveling solvent method during the growth gave a more stable zone and produced a rod that looked consistent with a stable melt, as seen in Figure 2.1b. In addition, this growth attempt also utilized a slower growth rate (0.5 mm/hr) and a much slower heating rate to the melting point in an attempt to prevent overshooting the desired temperature region and subsequent decomposition. Powder X-ray diffraction of the growth over time, as seen in Figure 2.1a, shows a variable composition throughout the growth process. The presence of mostly $Fe_3PO_4O_3$ and $FePO_4$ with trace Fe_2O_3 suggests decomposition of the rod as the stoichiometry does not correspond to $Fe_3PO_4O_3$. This inconsistency is likely due to precipitation of the $FePO_4$ added to the flux pellet. If the feed rod, which is pure $Fe_3PO_4O_3$, were decomposing, the composition would be much richer in iron oxide, as the $FePO_4$ would remain molten and likely stay in the floating zone. As OFZ is the method most likely to produce large centimeter-scale crystals, further growths will be attempted. The laser diode optical floating zone at the PARADIM institute, available through submission of user proposals, may be another avenue for growth of this compound as temperature control and zone temperature profiling is far more precise than with xenon lamps.

2.2. Successful Growth by Chemical Vapor Transport

Vapor transport has been the only method by which single crystals of $Fe_3PO_4O_3$ have been grown. In this technique, polycrystalline powder of either the attempted growth material or its precursors ($FePO_4$ and Fe_2O_3) and a transport agent are loaded in a fused quartz tube and sealed under vacuum. The tube is heated in a defined temperature gradient; the charge and transport agent react to produce gaseous species by which the material is transported to the other and the reaction is reversed by the change in temperature, leading to deposition of the charge as single
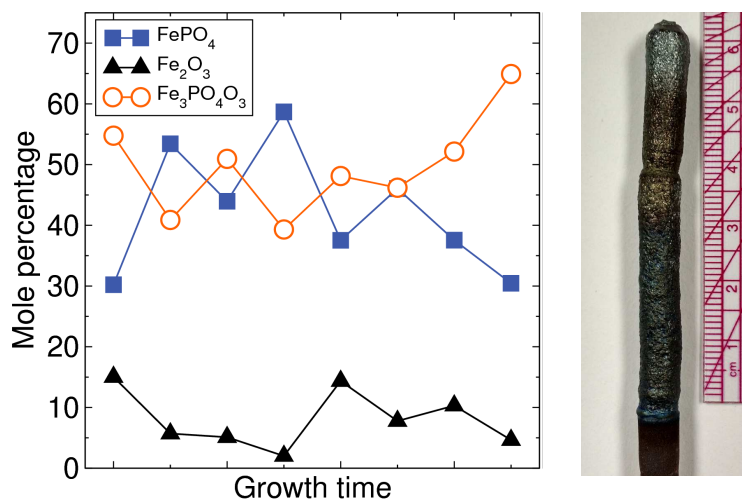
Figure 2.1: Results for optical floating zone growth of $Fe_3PO_4O_3$. a) Composition of the rod as a function of growth length; the left is the beginning of the growth. Composition is mostly $Fe_3PO_4O_3$ and $FePO_4$, but some Fe_2O_3 is also present. b) Image of the rod after growth. The color change of the rod does not seem to correspond to any major change in chemical composition.

crystals. An example transport equation for Fe_2O_3 with HCl is shown in Equation 2.1[30].

$$Fe_2O_3(s) + 6HCl(g) \rightleftharpoons 2FeCl_3(g) + 3H_2O(g) \tag{2.1}$$
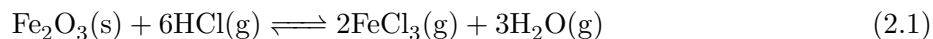
In order for vapor transport to be successful, the equilibrium constant must be close to 1; if it is too small, an insufficient partial pressure of the products will form and there will be extremely slow transport, and if it is too large, the gaseous species will not decompose to reform the reactants at the sink in the tube. These reactions can be either exothermic, in which the transport proceeds from cold to hot, or endothermic, in which materials transport hot to cold. In reality, determining the equilibrium reaction is difficult and is often based on empirical results or done computationally.

The first successful growth of $Fe_3PO_4O_3$ crystals documented here used a method similar to the literature[31], which called for transport using $FePO_4$ as a source with $ZrCl_4$ as a transport agent with the gradient 1000-900 °C (sink-charge). However, replication from our group was unsuccessful under these conditions. The successful reaction presented here uses the same charge and transport agent (160 mg $FePO_4$ and 149 mg $ZrCl_4$) with a temperature gradient 800-900 °C (charge-sink).

Table 2.1: Early chemical vapor transport growth attempts. First column shows transport agents, second shows transport conditions (temperatures are charge and sink, respectively), third is results: charge contents assessed by PXRD. All growths used $Fe_3PO_4O_3$ as the charge.

Transport agent	Temperature	Results
$FeCl_2/I_2$	850-750 °C	FeI_3 crystals; charge: Fe_2O_3, $Fe_3PO_4O_3$, FeP
$FeCl_3/P$	850-750 °C	Fe_2O_3 crystals; charge: Fe_2PO_5, Fe_2O_3
Fe/I_2	850-750 °C	Fe_2O_3 crystals; charge: $Fe_3PO_4O_3$ and Fe_2O_3
$FeCl_2/FeCl_3$	850-750 °C	$FeCl_3$ crystals; charge: $Fe_3PO_4O_3$ and Fe_2O_3
P/I_2 (PI$_3$ formed *in situ*)	850-750 °C	Fe_2O_3 crystals

While crystals did not grow by transport, a number of small 0.1-0.3 mm crystals did grow on the charge. They were confirmed by single crystal X-ray diffraction to be the desired phase, $Fe_3PO_4O_3$.

Several variables (temperature gradient, transport direction, charge, and transport agent amount) were tuned in an attempt to grow $Fe_3PO_4O_3$ crystals by transport with little success. Other transport agents from the literature[30] used in crystal growth of oxides, phosphates, and oxyphosphates were selected. A summary of attempted vapor transport results is provided in Table 2.1. The first column includes the transport agents; in all cases except the last, $Fe_3PO_4O_3$ was used as the charge to be transported. The temperature gradient indicated is the transport direction (the charge was placed at the hot end in all reactions). The products include any crystals formed by transport as well as XRD characterization of what was left in the charge. These were selected based on the observation of $FeCl_3$ crystals seen in attempted growths, suggesting it to be one of the gas-phase species responsible for transport. The combination of reducing and oxidizing agents suggested by the literature[30] was largely unsuccessful. In all cases there was degradation of the charge and crystal growth of some iron and oxygen containing species, but no successful $Fe_3PO_4O_3$ crystal growth. The use of phosphorus-rich $FePO_4$ as the charge may push the equilibrium towards including phosphorus in the species grown in these reactions.

Focusing on the reactions with $ZrCl_4$, these reactions were seeded with $Fe_3PO_4O_3$ crystals placed inside the tube before sealing. However, the larger crystals did not grow in the location that the growths were seeded, suggesting that the crystals re-dissolved and some other mechanism is

responsible for their growth. The crystals used for seeding were coated in Fluorolube, a fluorinated mineral oil, for storage and to prevent background issues that could be caused by hydrogen-based mineral oils if used in a neutron scattering experiment. A series of control experiments adding small amounts (< 1 mg) of Fluorolube®, Paratone oil, and PTFE powder to transport reactions resulted in crystal growth with Fluorolube and PTFE but no crystal growth with Paratone, suggesting that the addition of fluorinated organic compounds to the growth reaction is required for successful transport. A summary of these results can be seen in Table 2.2. This effect will need further experimentation to determine fluorine's role in the growth process.

Analysis of the growth reaction can lend insight into improvement of crystal quality. Powder X-ray diffraction of the charge from a successful transport reaction shows $FePO_4$, ZrP_2O_7, and Fe_2O_3 as the major species after the transport reaction. Droß suggests a reaction by which $Fe_3PO_4O_3$ transports[31]:

$$\frac{7}{3}FePO_4(s) + ZrCl_4(g) \rightleftharpoons ZrP_2O_7(s) + \frac{4}{3}FeCl_3(g) + \frac{1}{3}Fe_3PO_4O_3(s) \tag{2.2}$$
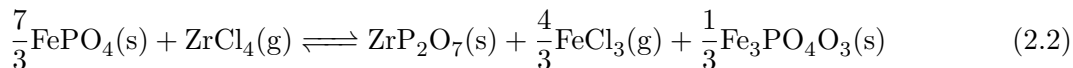
The presence of $FePO_4$ and ZrP_2O_7 in the charge and the presence of macroscopic $FeCl_3$ crystals provides evidence in support of Equation 2.2. The presence of Fe_2O_3 suggests P_2O_5 as the gas-phase species responsible for phosphorus transport by the following reaction:

$$4\,FePO_4(s) \rightleftharpoons 2\,Fe_2O_3(s) + P_4O_{10}(g) \tag{2.3}$$
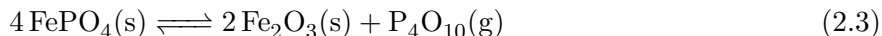
Any excess oxygen likely reacts preferentially with Zr as the molar enthalpy of formation for ZrO_2 is more favorable than that of Fe_2O_3; combination of ZrO_2 and P_2O_5 would lead to the zirconium pyrophosphate seen by PXRD. The use of $ZrCl_4$ as a transport agent is useful in two ways: 1) as a chlorine source for transport, and 2) as a sink for oxygen, keeping concentrations of iron chloride

18

Table 2.2: Summary of crystal growth reactions utilizing $FePO_4$ as a source and $ZrCl_4$ as a transport agent. All reactions were run with a temperature gradient of 920 °C-800 °C for 120 h.

Sample	Growth additive	Results
MJT1-97-1	No additive	0.2 mm $Fe_3PO_4O_3$ crystals on charge
MJT2-15-1	Fluorolube®-coated $Fe_3PO_4O_3$ crystals	0.5 mm $Fe_3PO_4O_3$ crystals
MJT2-3-3	< 1 mg Paratone® oil	No $Fe_3PO_4O_3$ crystals
MJT2-3-4	< 1 mg Fluorolube®	0.3 mm $Fe_3PO_4O_3$ crystals
MJT2-3-5	1 mg PTFE powder	0.3 mm $Fe_3PO_4O_3$ crystals

in the gas phase high. In addition, fluorine plays no role in this proposed reaction; the role of fluorine-containing species in this reaction mechanism will require further exploration as well as possible incorporation into the grown crystals.

The last major step in optimization of this growth is enlargement of grown crystals. The numerous small crystals present after growth suggests that nucleation is preferred. To grow larger crystals, there are two possible routes: 1) using more $FePO_4$ in the charge, or 2) reducing the degree of supersaturation of gas-phase precursors. The first may have undesired effects as the species present in the tube change over time, and this could change the equilibria. The second method could be achieved through alternative temperature profiles. Reaction 2-19-1 ramped over 5 h to 450 °C and then 96 h to the temperature gradient used previously (920 °C-800 °C). This did result in moderately larger crystals; however, a number of crystals appearing to be Fe_2O_3 were also present in with the $Fe_3PO_4O_3$ crystals. Using a greater concentration of $FePO_4$ will also be explored. Chemical vapor transport has shown significant promise as a method by which to grow crystals of $Fe_3PO_4O_3$ sufficient for use in single crystal neutron scattering experiments.

2.3. Experimental Method for Successful Crystal Growth

Iron phosphate hydrate ($FePO_4 \cdot xH_2O$, Alfa Aesar) was converted to the anhydrous form by heating overnight in air at 900 °C and stored in an argon-filled glovebox. $ZrCl_4$ (Acros Organics, 98%) was used without purification. Approximately 160 mg anhydrous $FePO_4$ and 148 mg $ZrCl_4$
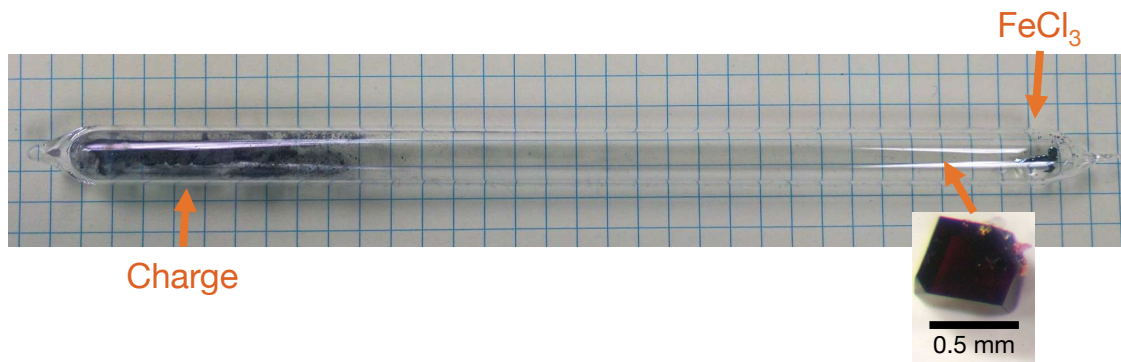
Figure 2.2: Image of a tube after CVT reaction, 21 cm in length. On the left is the source. Crystals are present in the right 4 cm of the tube (blown up in inset). The furthest right end contains large $FeCl_3$ crystals condensed out upon cooling.

were ground together in an argon-filled glovebox and placed in a 10x12 mm fused quartz tube as a loose powder. 2-4 $Fe_3PO_4O_3$ crystals from previous growths coated in Fluorolube were placed in the tube; the location does not seem to matter as long as they are sufficiently far from the open end as to not decompose upon sealing. The tubes were sealed to a length of 20-22 cm under < 10 mTorr vacuum. The source was placed at the thermocouple on one end of a three-zone furnace with the sink end at the thermocouple in the middle zone with the third zone kept at the same temperature as the middle zone. The furnace was ramped to the reaction temperature, 920 °C-800 °C-800 °C in 7.5 h and held for 120 h. The hot end was cooled over 12 h and the two cooler zones over 16 h to condense the $FeCl_3$ crystals at the source end away from the $Fe_3PO_4O_3$ growth region.

2.4. Conclusions

Small crystals of $Fe_3PO_4O_3$ have been successfully grown by chemical vapor transport reactions. While these are of sufficient size to study with neutron single crystal diffraction, larger crystals would allow for further measurements, including susceptibility and inelastic neutron scattering experiments. The initial work on chemical vapor transport has shown the merit of this method to grow crystals, and the experimental parameters simply need to be tuned to grow a smaller number

of larger crystals. Once successful, these could be combined with another method, such as seeded flux growth or seeded optical floating zone methods to grow very large single crystals.

3. Tuning the Antiferromagnetic Helimagnetism and Domain Size $Fe_3PO_4O_3$ by Magnetic Dilution[i]

3.1. Introduction

Magnetic frustration, arising from competing interactions, can lead to a variety of interesting phenomena. The roster of frustration-induced effects includes noncollinear spin structures[1,2], spin glasses[3], multiferroics[4], and spin liquids[5]. In each case, the delicate balance of interactions means that small perturbations, such as non-magnetic dilution, can lead to dramatic effects.

When frustration leads to helical magnetic structures, the possibility of the formation of Skyrmions arises[32]. Skyrmions are mesoscopic topological spin textures that show promise as a way to realize magnetic bubble memory[33]. They can form a thermodynamically stable Skyrmion-lattice phase[34–36] (also describable as a multi-k magnetic structure), or they can be generated as single defects, such as at the intersection of helical magnetic domain walls[37]. The presently-known materials forming Skyrmions are based on locally *ferromagnetic* or *ferrimagnetic* helical states, which are strongly influenced by small changes in an external magnetic field. This ferromagnetic background makes them susceptible to the Skyrmion hall effect, which hinders their efficient manipulation in devices[16]. Recent theoretical works suggest that *antiferromagnetic* Skyrmion devices (those based on an underlying antiferromagnetic helical state) would not suffer this drawback[13,16], though they have yet to be realized experimentally. In order to generate antiferromagnetic Skyrmions in a real material, one starting point may be the identification of an antiferromagnetic helical structure with a high density of domain walls.

---

[i] This chapter has been prepared as a manuscript for submission to the journal *Physical Review B*.

In this contribution we examine the magnetic order in gallium-doped $Fe_{3-x}Ga_xPO_4O_3$ through low temperature magnetic susceptibility and neutron powder diffraction. We use the helical magnetic structure that was previously proposed[24] to model the neutron powder diffraction patterns of the gallium-substituted materials. For low dilution, $0 \leq x \leq 0.25$, the decrease in helical pitch length can be reproduced using a reduced ratio of J_2/J_1 in the Heisenberg exchange model. This is consistent with a mean field picture, since twice as many J_2 interactions are broken as compared to the number of J_1 interactions for every Fe atom that is replaced with non-magnetic Ga. The size of the magnetic domains in the ab plane, determined via the broadening of magnetic Bragg peaks, is also reduced with increasing x. Curiously, the domain size appears to be constrained to be nearly equal to the pitch length. At higher values of gallium substitution, $x \geq 0.5$, long-range magnetic order is not observed.

3.2. Experimental

Polycrystalline samples in the solid solution series $Fe_{3-x}Ga_xPO_4O_3$ were prepared as previously described[24]. Fe_2O_3 and Ga_2O_3 were dried overnight at 600 °C and $FePO_4 \cdot nH_2O$ was converted to anhydrous $FePO_4$ by heating in air at 900 °C overnight in alumina crucibles, and then stored in an Argon-filled glovebox. Powder X-ray diffraction data were collected using a NaCl internal standard to check for purity and for shifts in the lattice parameter. Data were collected using a Bruker D8 Discover DaVinci Powder X-ray Diffractometer. Rietveld refinements including explicit modeling of the NaCl standard were performed using the TOPAS software package. Magnetization measurements were performed using a vibrating sample magnetometer in a Physical Properties Measurement System. The samples were measured in an applied field, $\mu_0 H = 1$ T, from $T = 1.8$ K to 300 K after cooling in the absence of an applied magnetic field (zero-field cooled measurement, ZFC), and then measured from 300-1.8 K in a 1T field (field cooled, FC).

Neutron powder diffraction measurements were carried out on 2.3-2.6 g polycrystalline samples of $x = 0$, 0.012, 0.25, 0.5, 1.0, and 1.5 using beamline HB-2A at the High Flux Isotope Reactor at Oak Ridge National Laboratory. The samples were measured at different temperatures from 3.5-295 K using a helium closed cycle refrigerator; collection temperatures were selected based on features observed in susceptibility measurements. The instrument provided a constant wavelength incident neutron beam with $\lambda = 2.4123$ Å from the Ge(113) monochromator, and 21 arcminute collimators were placed between the monochromator and the sample, while 12 arcminute collimators were used between the sample and the detectors. This configuration produces a resolution of $\Delta Q/Q = 2 \times 10^{-3}$. Magnetic and nuclear Rietveld refinements were performed using the FullProf software package[38].

Magnetic structures were determined for the (classical) $J_1 - J_2$ Heisenberg Hamiltonian for various ratios of J_2/J_1 using the numerical energy minimization routine implemented in the program SpinW[39]. This is implemented using a function which minimizes the Hamiltonian using the simplex method with periodic boundary conditions.

3.3. Results

The low-temperature magnetic susceptibility for all x as well as their neutron diffraction patterns at high and low temperatures is shown in Figure A.1. A slight splitting between the FC and ZFC curves in the parent compound ($x = 0$, not shown) begins slightly above T_N and persists down to at least 2 K. A more dramatic ZFC/FC splitting occurs for $x > 0.06$. Based on the neutron powder diffraction patterns, discussed next, this splitting occurs at the temperature T^* *below* T_N for $x = 0.25$, possibly indicating a freezing of remaining free spins in the material, likely at domain walls. For $x > 0.5$, a long-range ordered state is not observed, and the ZFC/FC splitting in the susceptibility might signal spin freezing throughout the entire sample. Accordingly, the temperature of the ZFC/FC splitting is denoted as T_F for $x > 0.5$.

Rietveld analysis of powder X-ray diffraction using an internal standard suggests solid-solution behavior of $Fe_{3-x}Ga_xPO_4O_3$. The extracted lattice parameters follow Vegard's law for solid solution between $Fe_3PO_4O_3$ and $Ga_3PO_4O_3$; the observed lattice parameters agree well with the extrapolated lattice parameters for a given value of x, suggesting that the actual composition reflects the nominal composition (Figure 3.3).

Neutron powder diffraction (NPD) confirms that the magnetic structures for $x > 0$ remain qualitatively similar to the parent compound, and confirms the decrease in T_N for these compounds as seen in Figure A.2. The disappearance of long-range order, which we characterize by absence of a well-formed magnetic peak near Q=1.35 Å^{-1}, is observed for $x \geq 0.5$. The ZFC/FC splittings for $x = 0.012$ and $x = 0.06$ correspond to T_N as best as can be seen in Figure A.2.

The helical magnetic structure model previously used for the parent compound, with an ordering wavevector $\mathbf{k}_h = (\delta_a, \delta_b, 1.5)$ (hexagonal setting of $R3m$) and needle-like finite size broadening indicating a magnetic domain size in the ab plane, was fit to the data for $0.012 \leq x \leq 0.25$. The magnitude of this incommensuration, $|\delta| = \sqrt{\delta_a^2 + \delta_b^2}$, increases with x, implying a reduced helical pitch length $l = \frac{a}{2\pi|\delta|}$ as illustrated in Figure 3.1b. The incommensuration is constant in temperature below T_N for each sample. For $x = 0.5$ at $T = 3.5$ K, the broad magnetic peaks are not visible and the normally sharp $(\delta_a, \delta_b, 3/2)$ peak at $Q = 1.35$ Å^{-1} is significantly broadened. For samples with $x \geq 1.0$, there are no magnetic Bragg features except for diffuse scattering centered at $Q = 1.35$ Å^{-1} as shown in Figures A.1 and 3.1.

The T_N decreases with gallium substitution, as deduced from both susceptibility and NPD data. The Bragg reflections from magnetic order disappear between 75 K and 140 K for $x = 0.25$, and for $x = 0.5$ the broad, flat-topped Bragg reflections are not observed, consistent with a spin-freezing transition in the dc susceptibility, as shown in Figure A.1. This decrease in T_N is often observed
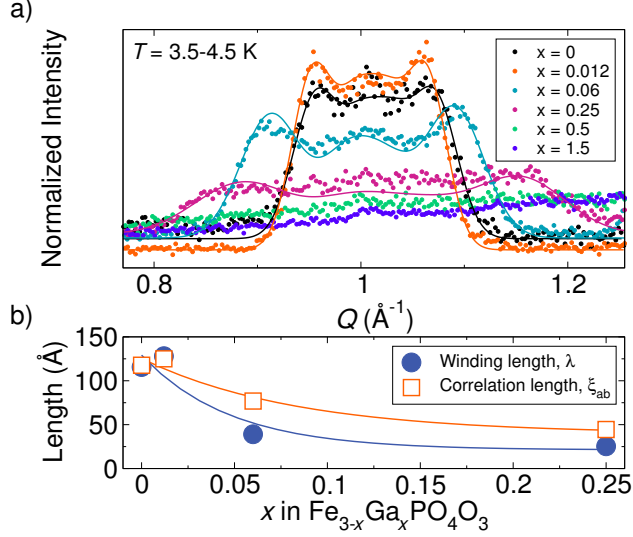
Figure 3.1: a) Magnetic Bragg peak for different gallium concentrations at 3.5-4.5 K; data is shown as points and the Gaussian, finite-size broadened fits as lines (see main text). The magnetic Bragg peak broadens and decreases in intensity with increased gallium content, consistent with a decrease in J_2 mean-field interaction strength relative to J_1 and domain size. b) Helical winding length and magnetic domain size are shown in the bottom panel as a function of gallium content; both decrease with gallium substitution. (Lines added to guide the eye.)

in magnetically diluted materials[40,41] and is attributed to the decrease in mean-field interaction strength.

Domain sizes can be extracted from the magnitude of the peak broadening required to match the slopes of the edges of the broad magnetic features. The coexistence of a sharp, resolution limited magnetic Bragg peak (near 1.35 Å^{-1}) and broad, flat topped peaks (such as that near 1 Å^{-1}) can be described by anisotropic broadening applied to peaks with large components in the ab plane (i.e., needle broadening). The Lorentzian needle broadening employed in the Fullprof refinement software package does not accurately capture the shape of the broad peaks, particularly the slopes of the peak edges. In order to extract the correlation length more accurately, we used a custom program written in MATLAB® which fits the lowest Q broad peak and the sharp peak simultaneously, applying a Gaussian broadening beyond the instrument resolution to the former, but not the latter; the peak intensities are permitted to refine independently (i.e., the intensities are not model-dependent) but the peak locations are defined by a single magnetic propagation vector.

The total Gaussian width is taken as the sum of the resolution and the broadening, consistent with a convolution of two Gaussians. This method allows us to refine the ordering wavevector, which is strongly constrained by the Q of the sharp peak, and the correlation length ξ_{ab} simultaneously. These fits are shown in Figure 3.1, while the fits to the whole NPD pattern obtained using Lorentzian broadening as implemented in Fullprof are shown in Figure A.3. The correlation length is extracted as $\xi_{ab} = 1/\Gamma$, where Γ is the half width at half maximum (HWHM) of the broadening Gaussian. The domain size decreases with increasing x, and is approximately equal to the helical pitch length for all values of x (Figure 3.1). The marked increase in domain density (from 0.0065 nm^{-2} at $x = 0$ to 0.043 nm^{-2} at $x = 0.25$) shows that magnetic dilution greatly stabilizes the formation of domain walls.

3.4. Discussion

The magnetic frustration in $Fe_3PO_4O_3$ stems from the competition between the antiferromagnetic intra-triangle J_1 and inter-triangle J_2 interactions. As non-magnetic gallium substitutes into the structure, the magnetic J_2 and J_1 interactions are disrupted. For each gallium atom, two J_1 interactions and four J_2 interactions are broken, from which we expect a reduction in the average ratio J_2/J_1. The effect of this rebalancing of the exchange interactions was examined using a numerical minimization of the classical spin Hamiltonian,

$$\mathcal{H} = \sum_{<i,j>} J_1 \mathbf{S}_i \cdot \mathbf{S}_j + \sum_{<i,k>} J_2 \mathbf{S}_i \cdot \mathbf{S}_k \tag{3.1}$$

where the first sum is over nearest neighbors and the second is over next nearest-neighbors.

Planar helical magnetic structures with the $\mathbf{k}_h = (\delta_a, \delta_b, 1.5)$ ordering wavevector were produced when $J_2/J_1 \approx 2$. The ratio of J_2/J_1 was varied slightly, and the resulting helical modulation ($|k_{ab}| = \frac{2\pi}{a}\delta$) was determined. The variation in the helical pitch of the magnetic structure agrees
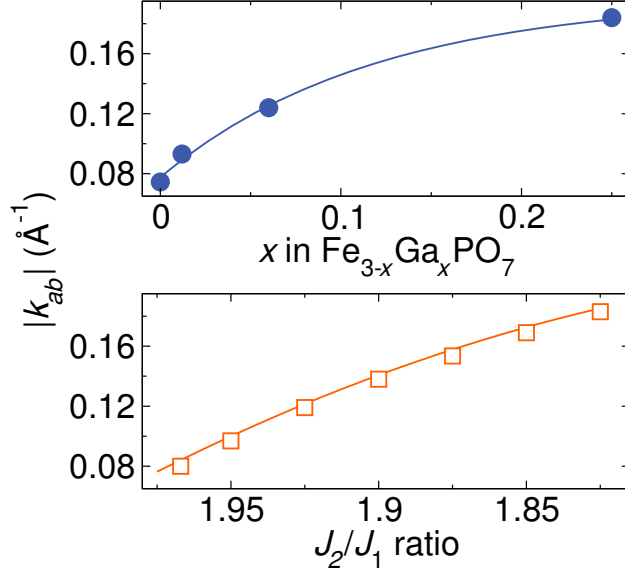
Figure 3.2: Experimental and calculated values of $|k_{ab}|$ for Ga-doped Fe_3PO_7. The mean-field model of decreased J_2/J_1 ratio with increased gallium substitution is consistent with experimental results. (Lines added to guide the eye.)

qualitatively with the experimental results: $|k_{ab}|$ increases with decreasing J_2/J_1, as shown in Figure 3.2. Matching the calculated $|k_{ab}|$ to that of the parent compound ($|k_{ab}| = 0.073$ Å^{-1}), this approximation gives $J_2/J_1 = 1.96$ for $x = 0$ which is reduced to $J_2/J_1 = 1.84$ for $x = 0.25$, indicating that the mean J_2 interaction strength is reduced relative to J_1, as expected.

We note that the assumed magnetic structure, as well as the Heisenberg model used above, is oversimplified. Within the constraints of our powder averaged neutron diffraction data, we cannot distinguish between this coplanar (helical) versus non-coplanar (conical) magnetic structures, as discussed in Reference 1. Furthermore, the lattice lacks any inversion center, implying the existence of Dzyaloshinskii-Moriya interactions for every pair of Fe atoms, which may favor non-coplanar structures. However, despite these shortcomings, the simple model presented here captures the main features of the NPD of $Fe_3PO_4O_3$ and its variation with magnetic dilution.

The neutron powder diffraction data of the solid solution series also lends insight into the unusually broad magnetic reflections. In the 2015 *Phys. Rev. B* article, the peaks were modeled as a single-wavevector structure with Gaussian broadening due to finite domains in the *ab* plane[24].
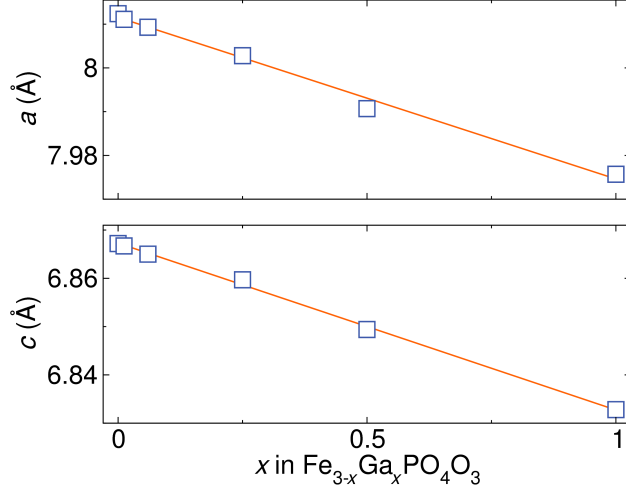
Figure 3.3: Extracted lattice hexagonal parameters, a (top panel) and c (bottom panel) from Rietveld refinements against room-temperature laboratory X-ray diffraction data, collected using NaCl as an internal standard. The orange lines are the interpolation between the previously reported values for $Fe_3PO_4O_3$[24] and $Ga_3PO_4O_3$[42].

In addition, models with multiple wavevectors, a square-wave incommensurate structure, and a conical structure were tested, each with less satisfactory modeling of the magnetic peak shape. We note that the broad peaks are more symmetric than expected with a magnetic form factor and a single ordinary wavevector, and this becomes even more pronounced with the significantly broader peaks such as those in $Fe_{2.75}Ga_{0.25}PO_4O_3$. This can be seen in Figure 3.1 in the difference between the single-wavevector model (solid line) and experimental data (points); the broad peaks in the model still have significant internal structure even with Gaussian broadening from the finite domains and the several symmetry-related wavevectors. Any attempt to add further broadening, either Lorentzian or Gaussian, results in less satisfactory modeling of the slopes on the peak sides.

As for the intensity of the flat-topped peak, there are multiple possible explanations. Spin covalency reduces the magnetic form factor, and the covalency seen in $Fe_3PO_4O_3$ could cause a decrease as observed in NiO[43]. In addition, the question of internal structure of the powder-averaged broad feature was left unanswered after the previous report[24]. The totally flat-topped peaks do not show the individual peaks from a single-**k** structure that would expected; the continuous- or multi-**k** structure proposed in the initial paper seems more likely, but cannot be discerned with polycrys-

29

talline specimens. Single-crystal neutron diffraction is required to fully elucidate the magnetic structure.

One other interesting feature in the parent compound is the presence of needle-like domains, manifested in the Lorentz broadening in any magnetic peaks with a component in the ab plane. As seen in Figure 3.1, the domain sizes decrease with gallium content. Magnetostriction has been proposed as an origin for the formation of antiferromagnetic domains[44,45]. Therefore, the presence of smaller Ga ions in the lattice may create strain or chemical pressure that increases the influence of any magnetostriction. This can be thought of as the nucleation or pinning of domain walls by non-magnetic impurities. Figure 3.1b seems to show a similar trend between the magnetic domain size and the helical winding length, suggesting that these unique domain walls are intimately related to the frustration also resultant in the helimagnetism. The presence of non-magnetic impurities could also lower the formation energy of domain walls; however, the mechanism by which these domain walls would be stabilized is still not understood, nor how they are energetically favorable[45]. Again, single crystal measurements to remove the effects of powder averaging will help lend insight into the domain structure of $Fe_3PO_4O_3$, which becomes more pronounced with gallium substitution.

3.5. Conclusions

The highly frustrated gallium-doped $Fe_{3-x}Ga_xPO_4O_3$ shows a continuous transition from a helical magnetic structure to a helical-like structure with decreased winding length and domain size, and finally to a spin-glass-like state with no long range order as gallium content increases. Based on numerical mean-field analysis of a $J_1 - J_2$ Hamiltonian, this stems from the change in the energetically similar competing interactions within the material. In addition, the anisotropic domains present in the parent compound, $Fe_3PO_4O_3$, decrease in size as gallium content increases, suggesting nucleation or pinning of domain walls at non-magnetic defects. The single-**k** structure used to model the magnetic diffraction of the parent compound is roughly consistent with the NPD

data at low values of x. As gallium content increases, the broad, flat-topped Bragg peaks do not show any internal structure, suggesting that a model with multiple magnetic propagation vectors is more representative. In either case, single crystal neutron diffraction will be required to fully determine both the domain behavior and magnetic structures in $Fe_3PO_4O_3$. While the cause of domains is still unknown in this compound, the change in domain size with gallium substitution upholds the idea that this material could be a model compound for studying the effects of domain architecture in magnetic materials with topological spin textures[13].

4. Magnetism in $Fe_3PO_{7-x}F_x$

4.1. Introduction

Fluorides and oxyfluorides have long been a topic of research due to the fluoride anion's small, "hard" ionic character[46]. The novel properties arising from this include fast ionic conductivity in LaF_3[47], unique optical properties due to its low polarizability[48], and low-friction mechanical properties. The π-donor characteristics make it similar to oxygen in its abilities to stabilize high-spin metal centers and facilitate superexchange interactions in magnetic ions. In addition to fluorides, oxyfluorides can form with either stoichiometric ratios (such as pyrochlore, $Ca_2Nb_2O_6F$) or as a solid solution due to their similar ionic radii as seen in the superconductor $La_2CuO_4F_\delta$. The physical properties of these compounds can be tuned and changed, such as with $WO_{3-x}F_x$[49]. The oxide is an insulating material with a monoclinic unit cell, but upon fluorination, the material goes from the monoclinic unit cell through tetragonal to a cubic unit cell and sees a transition from insulating to metallic and finally superconductivity emerges with sufficient fluorine content. One of the most studied families of oxyfluorides is the cuprate superconductors. Fluorination of $HgBa_2Ca_2Cu_3O_8$ shows an increase in T_c from 4 to 138 K, two orders of magnitude[50]. The insertion of fluorine anions results in both a change in oxidation state of copper and rearrangement of the Cu-O planes believed responsible for superconductivity. The ability to easily tune O^{2-}/F^- concentrations allows for an experimental handle to control many of the desirable electronic properties in transition metal compounds.

Fluorides are less studied than oxides due to practical reasons; the traditional methods for preparing fluorides often involve F_2 gas or HF as fluorinating agents, both of which have significant toxicity towards humans. Recent literature has made use of low-temperature chimie douce reactions

32

with decomposing fluoride sources such as polytetrafluoroethylene (PTFE), polyvinylidene fluoride (PVDF), xenon difluoride (XeF_2), or phosphorus trifluoride (PF_3). These have several advantages: milder reaction condititons, such as the ability to perform PTFE decomposition fluorinations in air, safer reaction precursors and byproducts, and decomposition temperatures of $< 500°C$, which allows for the formation of metastable oxyfluorides. Some reactions include fluorination of WO_3 with PTFE as a fluorine source[49], Nd_2CuO_4 with XeF_2[51], or $Ba_2Fe_2O_5$ with PVDF to give the anion-ordered perovskite $Ba_3Fe_3O_7F$[52]. These different fluorine sources allow for the use of low-temperature reactions that make fluorine chemistry significantly less dangerous. One downside is that the relationship between precursor amount and final fluoride content is often non-linear, making targeted stoichiometries more difficult.

The literature has focused recently on the insertion of fluoride anions into lattices, especially with respect to the cuprate superconductors. In their 1998 review, Greaves and Francesconi propose three possible reactions upon fluorination[53]:

1. Substitution of one fluoride anion for one oxide anion, resulting in reduction of the metal lattice,

2. Incorporation of two fluoride anions for one oxide anion, causing no change in oxidation state but doubling the number of anions, and

3. Insertion of fluoride anions into interstitial sites, causing oxidation of the metal lattice.[53]

In addition to these three points, McCabe and Greaves suggest that structural rearrangement following fluorination is another commonly seen consequence[54]. By correct choice of fluorinating agent and reaction temperature, it is possible to get different effects in the same material, such as in the lanthanide cuprates, Ln_2CuO_4. One paper studying the effects of fluorine incorporation and the effects on the structural transformations in Nd_2CuO_4 uses XeF_2 as a fluorine source[51].

This allows for significantly lower reaction temperatures than that of other flourine sources due to its lower decomposition temperature, 119°C for XeF_2 as compared to 260 °C for PTFE. At low reaction temperatures, below 300 °C, fluorine is inserted into interstitials, resulting in the oxidation of copper, $Nd_2CuO_4F_x$[51]. Higher temperatures in the 300-400 °C range result in anion exchange and the compounds $Nd_2CuO_{3.6}F_{0.8}$ and $Nd_2CuO_3F_2$, both of which have a structural rearrangement from the parent oxide[51]. One issue discussed by the authors is the significant inhomogeneity in fluorine content from these reactions. The low temperatures that allow for metastable phases to form also preclude structural rearrangement, leading to non-uniform fluorine content by domain. In superconductivity and magnetism, two of the main applications of these oxyfluorides, the sample inhomogeneity leads to significant issues when trying to determine structure-property relationships.

In this study, $Fe_3PO_4O_3$ is fluorinated with PTFE in order to study the effects of fluorine incorporation on the magnetic properties. Initial results by powder X-ray diffraction, neutron powder diffraction, magnetic susceptibility, and isothermal magnetization show that there seems to be no structural rearrangment upon fluoride incorporation in the lattice. The helical magnetic structure of the parent compound seems to be preserved, but the characteristic broad, flat-topped magnetic reflections discussed in Chapter 1 are narrower and more intense. The susceptibility shows several additional features not present in the parent compound, suggesting a rich magnetic phase diagram. The location of fluorine within the lattice is still unknown, but the possible locations within the lattice are discussed in the framework of the preliminary diffraction measurements.

4.2. Experimental

$Fe_3PO_4O_3$ was prepared as described previously[24] and washed with 0.1 M HCl overnight to remove $FePO_4$ impurities. Fluorinated samples were prepared by low temperature reactions of $Fe_3PO_4O_3$ and PTFE. Samples were lightly ground with a mortar and pestle and placed in fused quartz tubes as a loose powder. Tubes were heated at 5°C/min to 350-450 K, held for 36 h, and
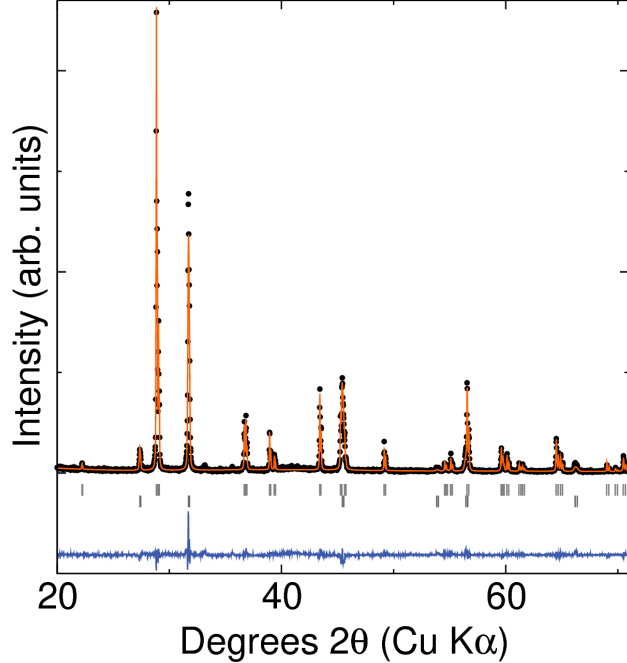
Figure 4.1: Room-temperature laboratory X-ray powder diffraction of fluorine-doped $Fe_3PO_4O_3$ with a NaCl standard. There are no major impurity peaks and the pattern is well-described by the same model as the parent compound. The top row of tick marks are for $Fe_3PO_4O_3$ and the bottom row for the NaCl standard.

furnace cooled to room temperature. Tubes were oriented in the furnace such that the powder remained at the hot end as to prevent condensation of pyrolysis byproducts on the sample.

Powder X-ray diffraction data were collected using a NaCl internal standard to check for purity and shifts in the lattice parameter using a Bruker D8 Discover DaVinci Powder X-ray Diffractometer. Rietveld refinements including explicit modeling of the NaCl standard were performed using the TOPAS software package. Magnetization measurements were performed using a vibrating sample magnetometer in a Physical Properties Measurement System. The samples were measured in an applied field, $\mu_0H = 0.1$ T, from $T = 1.8$ K to 300 K after cooling in the absence of an applied magnetic field (zero-field cooled measurement, ZFC), and then measured from 300-1.8 K in a 1000 Oe field (field cooled, FC). Five-quadrant isothermal magnetization measurements were performed at field strengths up to 14 T. The sample was cooled to the desired temperature, the field was swept to the positive maximum field strength, down to the negative maximum field strength, and back

to the positive maximum field strength. The sample was brought up above the Néel temperature before all magnetization measurements.

Samples for neutron powder diffraction required larger masses than could be prepared in one tube, so approximately 3 g of $Fe_3PO_4O_3$ and the appropriate amount of PTFE powder were homogenized and sealed in six tubes; all masses were within 2 mg of each other. These were all reacted in the same furnace in an attempt to keep the sample homogenous. Neutron powder diffraction was performed on beamline BT-1 at the NIST Center for Neutron Research, NIST National Laboratory, Gaithersburg, Maryland. The samples were measured at different temperatures ranging from 3.5-295 K using a helium closed cycle refrigerator; temperatures below T_N were also measured in a 7 T magnetic field from a superconducting magnet. The instrument provided a constant wavelength incident neutron beam with $\lambda = 2.078$ Å from the Ge(113) monochromator. A 60 arcminute collimator was used before the monochromator, 20 arcminute in-pile collimators were placed between the monochromator and the sample, and 7 arcminute collimators were used between the sample and the detectors to maximize flux. Magnetic and nuclear Rietveld refinements were performed using the FullProf software package[38] and a custom script written in MATLAB®.

4.3. Results and Discussion

Laboratory powder X-ray diffraction of fluorinated $Fe_3PO_4O_3$ is shown in Figure 4.1 for a reaction of 15 wt% PTFE reacted at 350 °C for 36 h. The data is well-described by the model of the parent compound. Use of the NaCl standard gives lattice parameters of $a = b = 8.0126$ Å and $c = 6.8672$ Å, a negligible increase as compared to the parent compound with the same standard, $a = b = 8.0124$ Å and $c = 6.8762$ Å. This suggests no major structural rearrangement.

Magnetic susceptibility of fluorine-doped $Fe_3PO_4O_3$ is significantly different from that of the parent compound. A sharp peak with field-dependent transition temperature near $T = 13$ K is present, as well as a defined ZFC/FC splitting at $T = 78$ K. The Néel transition in the parent

36
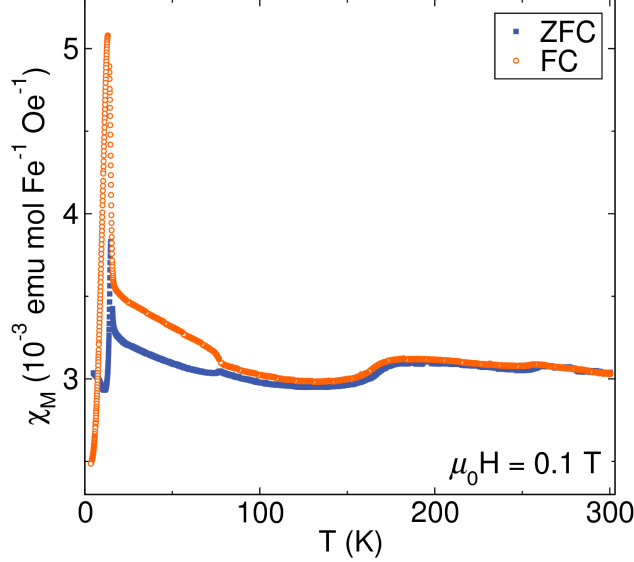
Figure 4.2: Zero-field cooled and field cooled magnetic susceptibility of fluorine-doped $Fe_3PO_4O_3$ at field $\mu_0 H = 0.1$ T. The data shows a sharp peak near $T = 13$ K, a ZFC/FC splitting at $T = 78$ K, and a Néel transition at $T = 161$ K similar to that of the parent compound. Deviations above 225 K are due to measurement anomalies.

compound is still present, but at a slightly lower temperature of 161 K. A Curie-Weiss analysis has also been performed for $200 < T < 300$ K. The region of fitting is not completely linear, demonstrating the presence of short-range magnetic interactions, but with a χ_0 term the fit is not unreasonable. Fluorinated $Fe_3PO_4O_3$ has a Curie temperature of -1643 K and $p_{eff} = 5.46$; these numbers show the fit is not valid as $T << |\theta_{CW}|$, but qualitatively suggest the interactions are still strong and antiferromagnetic.

Figure A.4 shows the isothermal magnetization at $T = 7, 13, 16, 50$ K. Even at very high magnetic fields of 14 T, the magnetization does not saturate. One interesting feature is the virgin curve shown in orange lying outside the narrow hysteresis loop at temperatures below 13 K, suggesting the formation of a kinetically trapped magnetic state. There is also a kink in the susceptibility near a field strength of ± 5 T, suggesting a transition in the magnetic structure. At $T = 13$ K (the location of the sharp peak in the susceptibility) a hysteresis loop opens, suggesting some difference in magnetic order at this temperature. In the region of 13 K $\leq T \leq 78$ K, where the ZFC and FC curves are split, the hysteresis loop closes and the virgin curve again lies slightly outside of the
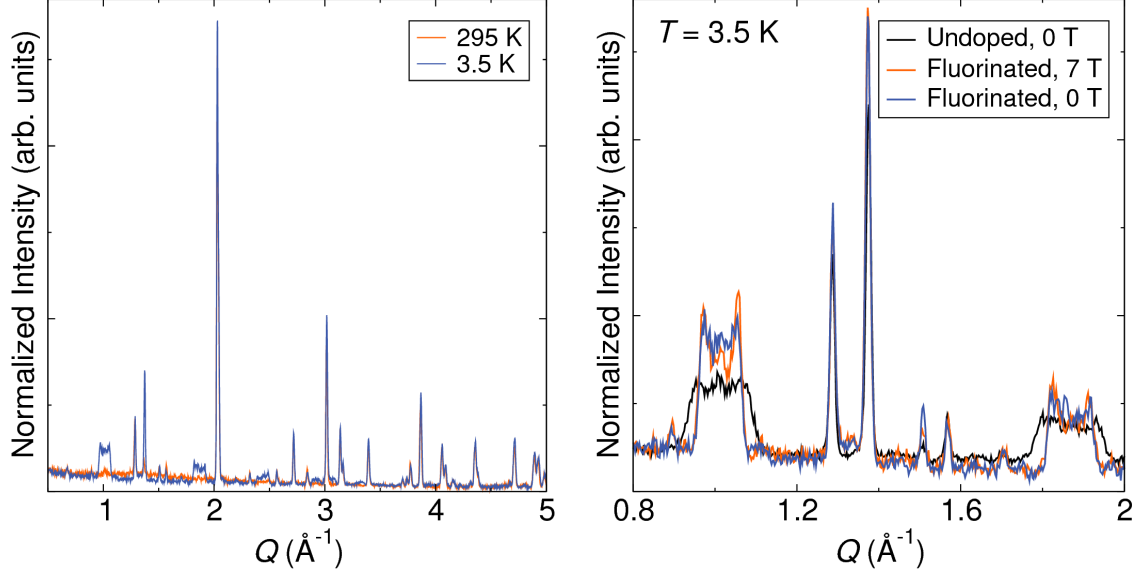
Figure 4.3: a) Full neutron powder diffraction patterns of $Fe_3PO_{7-x}F_x$ at $T = 3.5$ K in blue and $T = 295$ K in orange. The broad, flat-topped magnetic peaks are visible to higher Q than in the parent compound. b) Zoomed in region of neutron powder diffraction at $T = 3.5$ K of undoped $Fe_3PO_4O_3$ in black, fluorinated $Fe_3PO_4O_3$ at 0 T in blue, and $Fe_3PO_4O_3$ at 7 T in orange. The broad, flat-topped magnetic peaks in the fluorinated compound are taller and narrower than in the undoped parent compound.

other traces. This effect is more apparent at $T = 50$ K. The magnetization is linear, suggesting antiferromagnetic order as in the parent compound.

Neutron powder diffraction of the compound is shown in Figures 4.3 and 4.4. The left panel shows the data at $T = 3.5$ K and $T = 295$ K under zero field. The diffraction is similar to the parent compound, featuring the same broad, flat-topped magnetic reflections; however, these are more prominent and visible to higher Q than in the parent compound. Figure 4.3b highlights the major differences in the diffraction patterns. The broad magnetic reflections are narrower and have greater intensity in the fluorinated compound. The increased intensity, as from an increase in moment could be attributed to a decrease in covalency with the substitution of oxygen for fluorine as the latter is much more electronegative. The application of a magnetic field also results in sharpening of the peaks near the edges of the broad, flat-topped peaks, suggesting a preferred wavevector rather than a continuum of wavevectors. As in the gallium-doped compounds, the features in the magnetic susceptibility do not seem to correlate to any sort of magnetic transition
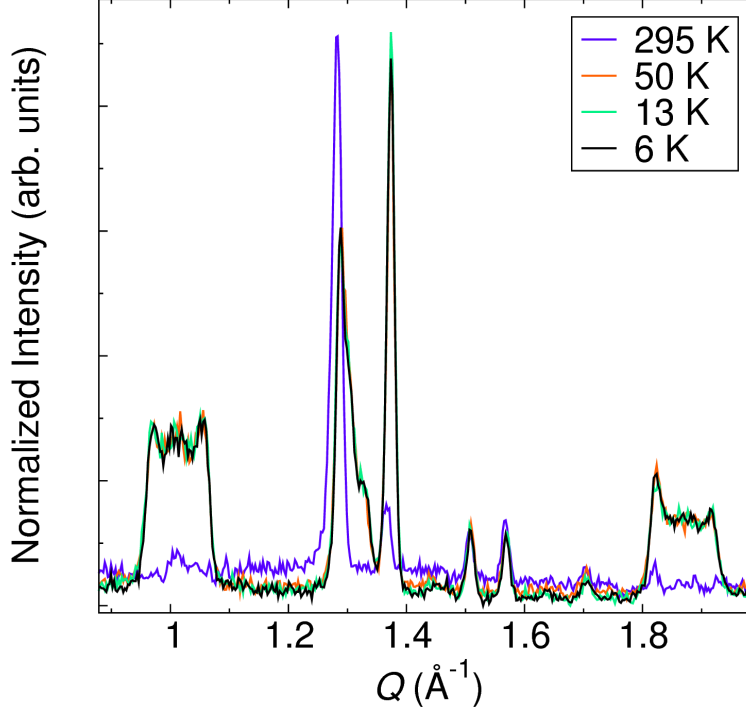
Figure 4.4: Zoomed-in region of NPD data for all measured temperatures in fluorine-doped $Fe_3PO_4O_3$. The diffraction data is constant below T_N. In addition, the reflection at $Q = 1.28$ Å^{-1} is split in only one sample, suggesting issues with inhomogeneity.

seen by neutron powder diffraction. The ZFC/FC splitting seen in the magnetic susceptibility is reminiscent of the T^* transition seen in $Fe_{2.75}Ga_{0.25}PO_4O_3$. Figure 4.4 shows no temperature dependent changes below T_N as in the parent compound. In addition, the peak at $Q = 1.28$ Å^{-1} is split in this sample below the ordering temperature, which may be suggestive of inhomogeneity in the specimen.

A simulation of the $T = 3.5$ K NPD data to model the magnetic structure is shown in Figure 4.5. The magnetic Bragg reflections are well-modeled by the single wavevector magnetic structure with anisotropic broadening. The magnitude of the **k** vector in the ab plane is decreased from the parent compound, $k_{mag} = 0.0519$ Å^{-1}. Both the helical winding length, $\lambda = 175.3$ Å, and the correlation length, $\xi_{ab} = 166.7$ Å, are greater than in parent compound ($\lambda = 86$ Å, $\xi_{ab} = 70$ Å). Interestingly, the two are still almost equal, as seen in the gallium-substituted solid solution series and discussed in Chapter 3.
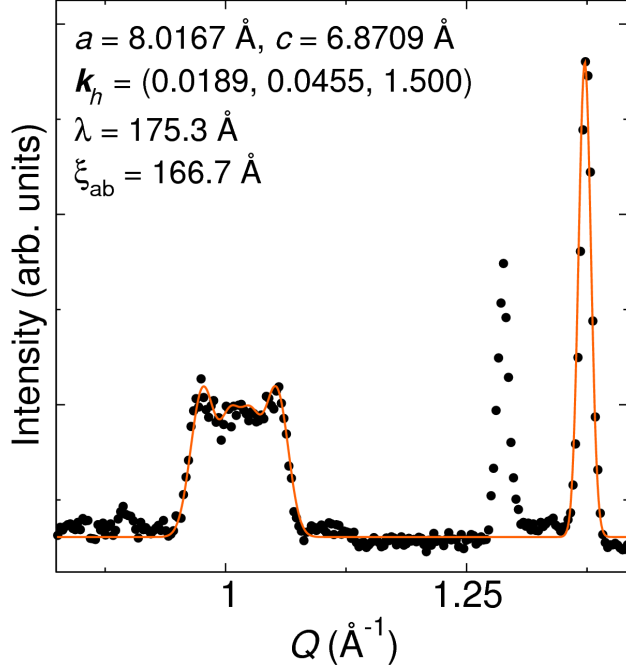
Figure 4.5: Calculation of the magnetic structure using the custom MATLAB® script discussed in Chapter 3 as compared to NPD at $T = 3.5$ K. Both the helical winding length and correlation length are larger for the fluorine-doped compound.

The fluoride concentration in this compound is still unknown. ICP-OES after careful HF digestion will likely be required to quantify the fluorine and oxygen content. Once this is known, the method of incorporation and location of fluorine within the lattice can be narrowed down. Mössbauer spectroscopy on the powders could also be informative, as it would reveal any changes in crystal field environment or oxidation state of the iron atoms. Preliminary data shows that the fluorine-doped compound is different than the parent and these measurements will be required to determine the origins of the novel properties.

4.4. Conclusions and Future Directions

Incorporation of fluorine into $Fe_3PO_4O_3$ produces a marked change in the magnetic properties based on magnetic susceptibility, isothermal magnetization, and neutron powder diffraction characterization. The helical structure proposed for the parent compound seems to be preserved, though the magnetization and susceptibility show several additional features not corroborated by

the NPD. The winding length and correlation lengths seem to increase as compared to the parent compound, though they are roughly equal.

While single crystals are required for conclusive determination of the magnetic structure in $Fe_3PO_{7-x}F_x$, there is still substantial work that could be performed on the powders available. Mössbauer spectroscopy would give valuable information on the crystal field seen by the iron sub-lattice. Full or partial reduction of Fe^{3+} to Fe^{2+} could help explain the novel magnetic properties seen in the fluoride. It could also help identify the location of fluorine within the lattice. Measurement of the fluoride content with ICP-OES would tell whether there are small amounts of fluorine substitution or full anion exchange and ordering within the lattice.

Single crystal growth of this compound is likely untenable by traditional methods for this compound, as solid state preparation was unsuccessful, likely due to metastability. As such, it may be more feasible to fluorinate single crystals after growth. There are substantial issues with homogeneity with this method, as it would require significant diffusion to the center of crystals. High quality fluorinated single crystals might never be obtained. In such a case, neutron scattering from single crystals of the parent compound may lend insight into the change in magnetic properties described here.

Bibliography

[1] Yoshimori, A. *J. Phys. Soc. Jap.* **1959**, *14*, 807–821.

[2] Kaplan, T. A. *Phys. Rev.* **1959**, *116*, 888–889.

[3] Itoh, M.; Natori, I.; Kubota, S.; Motoya, K. *J. Phys. Soc. Jap.* **1994**, *63*, 1486–1493.

[4] Blake, G. R.; Chapon, L. C.; Radaelli, P. G.; Park, S.; Hur, N.; Cheong, S.-W.; Rodríguez-Carvajal, J. *Phys. Rev. B* **2005**, *71*, 214402.

[5] Shimizu, Y.; Miyagawa, K.; Kanoda, K.; Maesato, M.; Saito, G. *Phys. Rev. Lett.* **2003**, *91*.

[6] Freedman, M. H.; Kitaev, A.; Larsen, M. J.; Wang, Z. *Bulletin of the American Mathematical Society* **2002**, *40*, 31–39.

[7] Lee, P. A. *Reports on Progress in Physics* **2007**, *71*, 012501.

[8] Nagata, S.; Keesom, P. H.; Harrison, H. R. *Physical Review B* **1979**, *19*, 1633–1638.

[9] Dekker, C.; Arts, A. F. M.; de Wijn, H. W. *Physical Review B* **1988**, *38*, 11512–11522.

[10] Ramirez, A. P.; Hayashi, A.; Cava, R. J.; Siddharthan, R.; Shastry, B. S. *Nature* **1999**, *399*, 333–335.

[11] Morris, D. J. P.; Tennant, D. A.; Grigera, S. A.; Klemke, B.; Castelnovo, C.; Moessner, R.; Czternasty, C.; Meissner, M.; Rule, K. C.; Hoffmann, J.-U.; Kiefer, K.; Gerischer, S.; Slobinsky, D.; Perry, R. S. *Science* **2009**, *326*, 411–414.

[12] dos Santos Dias, M.; Bouaziz, J.; Bouhassoune, M.; Blügel, S.; Lounis, S. *Nature Communications* **2016**, *7*, 13613.

[13] Zhang, X.; Zhou, Y.; Ezawa, M. *Scientific Reports* **2016**, *6*, 24795.

[14] Blundell, S. *Magnetism in Condensed Matter (Oxford Master Series in Physics)*; Oxford University Press, 2001.

[15] Fert, A.; Cros, V.; Sampaio, J. *Nature Nanotechnology* **2013**, *8*, 152–156.

[16] Barker, J.; Tretiakov, O. A. *Physical Review Letters* **2016**, *116*, 1–5.

[17] Krause, S.; Wiesendanger, R. *Nature Materials* **2016**, *15*, 493–494.

[18] Wills, A. *Le Journal de Physique IV* **2001**, *11*, 133–158.

[19] Bragg, W. L. The structure of some crystals as indicated by their diffraction of X-rays. Proceedings of the Royal Society of London A: Mathematical, Physical and Engineering Sciences. 1913; pp 248–277.

[20] Sears, V. F. *Neutron News* **1992**, *3*, 26–37.

[21] Inc., Q. D. Model P850: PPMS Dilution Refrigerator System.

[22] Gavoille, G.; Gleitzer, C.; Long, G. J. *Revue de chimie minérale* **1987**, *24*, 42–55.

[23] Anderson, P. W. *Physical Review* **1950**, *79*, 350–356.

[24] Ross, K. A.; Bordelon, M. M.; Terho, G.; Neilson, J. R. *Physical Review B* **2015**, 134419.

[25] Modaressi, A.; Courtois, A.; Gerardin, R.; Malaman, B.; Gleitzer, C. *Journal of Solid State Chemistry* **1983**, *47*, 245–255.

[26] Shi, Q.; Zhang, L.; Schlesinger, M. E.; Boerio-Goates, J.; Woodfield, B. F. *Journal of Chemical Thermodynamics* **2013**, *62*, 86–91.

[27] Hill, A. H.; Jiao, F.; Bruce, P. G.; Harrison, A.; Kockelmann, W.; Ritter, C. *Chemistry of Materials* **2008**, *20*, 4891–4899.

[28] Plakhty, V. P.; Gukasov, A. G.; Papoular, R. J.; Smirnov, O. P. *Europhysics Letters (EPL)* **1999**, *48*, 233–239.

[29] Zhang, L.; Schlesinger, M. E.; Brow, R. K. *Journal of the American Ceramic Society* **2011**, *94*, 1605–1610.

[30] Binnewies, M.; Glaum, R.; Schmidt, M.; Schmidt, P. *Chemical Vapor Transport Reactions*; Walter de Gruyter, 2012.

[31] Droß, T. Diplomarbeit. M.Sc. thesis, University of Gießen, 1997.

[32] Nagaosa, N.; Tokura, Y. *Nature Nanotechnology* **2013**, *8*, 899–911.

[33] Sampaio, J.; Cros, V.; Rohart, S.; Thiaville, A.; Fert, A. *Nature Nanotechnology* **2013**, *8*, 839–844.

[34] Adams, T.; Chacon, A.; Wagner, M.; Bauer, A.; Brandl, G.; Pedersen, B.; Berger, H.; Lemmens, P.; Pfleiderer, C. *Physical Review Letters* **2012**, *108*, 1–5.

[35] Münzer, W.; Neubauer, A.; Adams, T.; Mühlbauer, S.; Franz, C.; Jonietz, F.; Georgii, R.; Böni, P.; Pedersen, B.; Schmidt, M.; Rosch, A.; Pfleiderer, C. *Physical Review B* **2010**, *81*.

[36] Pfleiderer, C.; Rosch, A.; Neubauer, A.; Georgii, R. *Science* **2009**, 915–920.

[37] Zhou, Y.; Ezawa, M. *Nature Communications* **2014**, *5*, 4652.

[38] Rodríguez-Carvajal, J. *Physica B* **1993**, *192*, 55–69.

[39] Toth, S.; Lake, B. *Journal of Physics: Condensed Matter* **2015**, *27*, 166002.

[40] B. Martínez, F. Sandiumenge, A. Rouco, A. Labarta, J. Rodríguez-Carvajal, M. Tovar, M.T. Causa, S. Galí,; Obradors, X. *Physical Review B* **1992**, *46*, 786–793.

[41] Få k, B.; Sadykov, R. a.; Flouquet, J.; Lapertot, G. *Journal of Physics: Condensed Matter* **2005**, *17*, 1635–1644.

[42] Boudin, S.; Lii, K.-H. *Acta Crystallographica Section C: Crystal Structure Communications* **1998**, *54*, 5–7.

[43] Owen, J.; Thornley, J. H. M. *Reports on Progress in Physics* **1966**, *29*, 675–728.

[44] Minakov, A.; Shvets, I.; Veselago, V. *Journal of Magnetism and Magnetic Materials* **1990**, *88*, 121–133.

[45] Gomonay, H.; Loktev, V. M. *Journal of Physics: Condensed Matter* **2002**, *14*, 3959–3971.

[46] Hagenmuller, P. *Inorganic Solid Fluorides: Chemistry and Physics*; Elsevier, 2012.

[47] Igel, J. R.; Wintersgill, M. C.; Fontanella, J. J.; Chadwick, A. V.; Andeen, C. G.; Bean, V. E. *Journal of Physics C: Solid State Physics* **1982**, *15*, 7215–7228.

[48] Lucas, J. *Journal of Fluorine Chemistry* **1995**, *72*, 177–181.

[49] Hirai, D.; Climent-Pascual, E.; Cava, R. J. *Physical Review B* **2011**, *84*, 174519.

[50] Lokshin, K. A.; Pavlov, D. A.; Putilin, S. N.; Antipov, E. V.; Sheptyakov, D. V.; Balagurov, A. M. *Physical Review B* **2001**, *63*, 064511.

[51] Hadermann, J.; Tendeloo, G. V.; Abakumov, A.; Rozova, M.; Antipov, E. *Journal of Solid State Chemistry* **2001**, *157*, 56–61.

[52] Clemens, O.; Reitz, C.; Witte, R.; Kruk, R.; Smith, R. I. *Journal of Solid State Chemistry* **2016**, *243*, 31–37.

[53] Greaves, C.; Francesconi, M. G. *Current Opinion in Solid State and Materials Science* **1998**, *3*, 132–136.

[54] McCabe, E. E.; Greaves, C. *Journal of Fluorine Chemistry* **2007**, *128*, 448–458.

A. Appendix
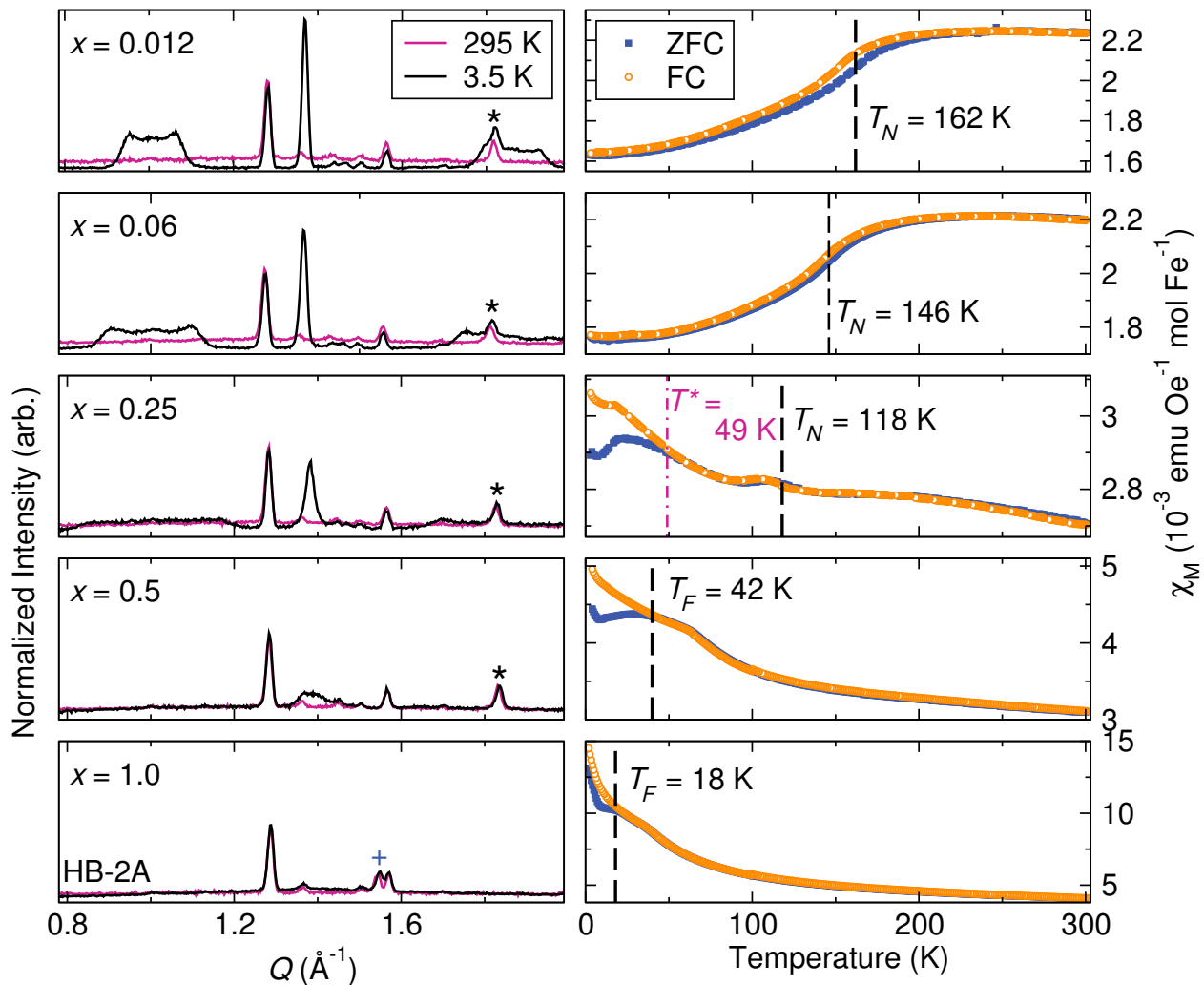
Figure A.1: Neutron powder diffraction (left) and magnetic susceptibility (right) for $x = 0.012, 0.06, 0.25, 0.5$, and 1.0 in $Fe_{3-x}Ga_xPO_4O_3$. The magnetic Bragg reflections centered at $Q = 1, 1.35, 1.75$ $Å^{-1}$ decrease in intensity and broaden as gallium content increases. The magnetic susceptibility shows a decrease in the magnetic transition temperature with increased gallium substitution and a shift to a ZFC/FC splitting suggestive of a frozen-spin state. The domain freezing transition in $x = 0.25$ is denoted as the pink dashed line. Small quantities of $FePO_4$ impurities in the NPD are shown as black stars and $GaPO_4$ impurities as blue addition signs.
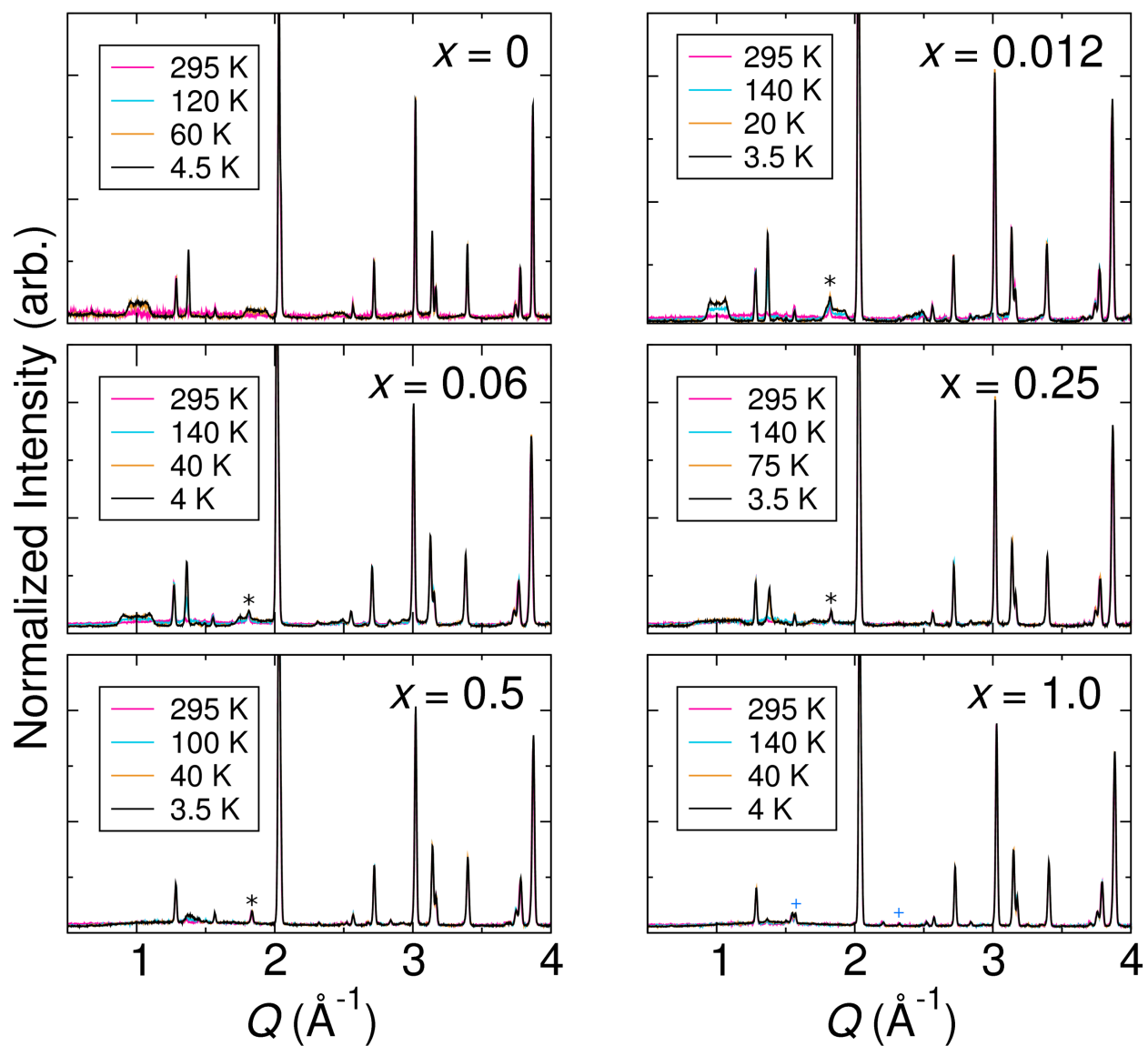
Figure A.2: Raw data from neutron powder diffraction of $Fe_{3-x}Ga_xPO_4O_3$ for the full range of Q at all temperatures and values of x. $FePO_4$ impurity peaks are denoted with black stars and $GaPO_4$ impurity peaks are denoted with blue addition signs.
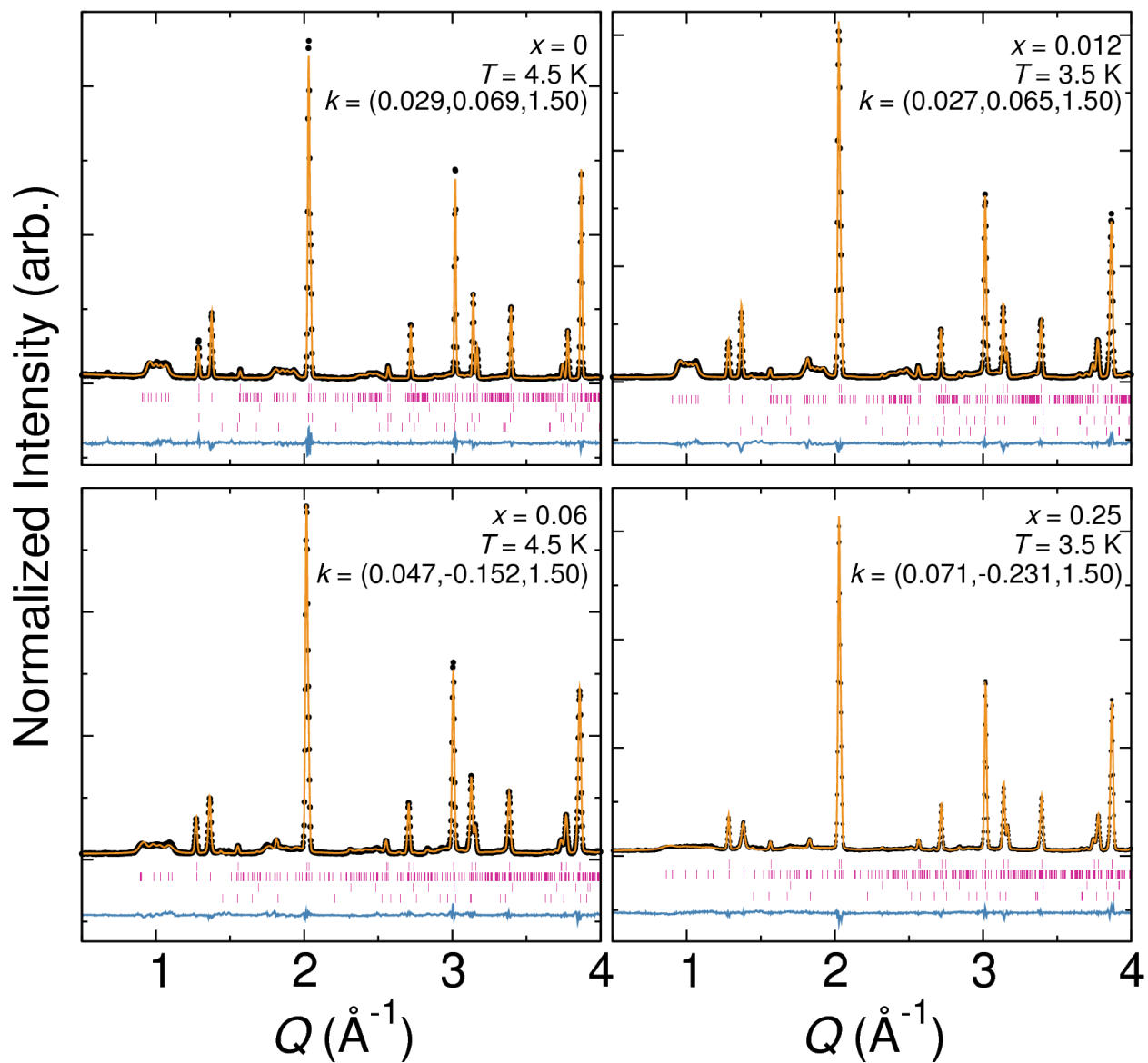
Figure A.3: All low-temperature magnetic Rietveld refinements for the solid solution series $Fe_{3-x}Ga_xPO_4O_3$. Data is shown as black points, the fit in orange, tick marks for the nuclear, magnetic, and impurity phases in pink, and the difference curve in blue.
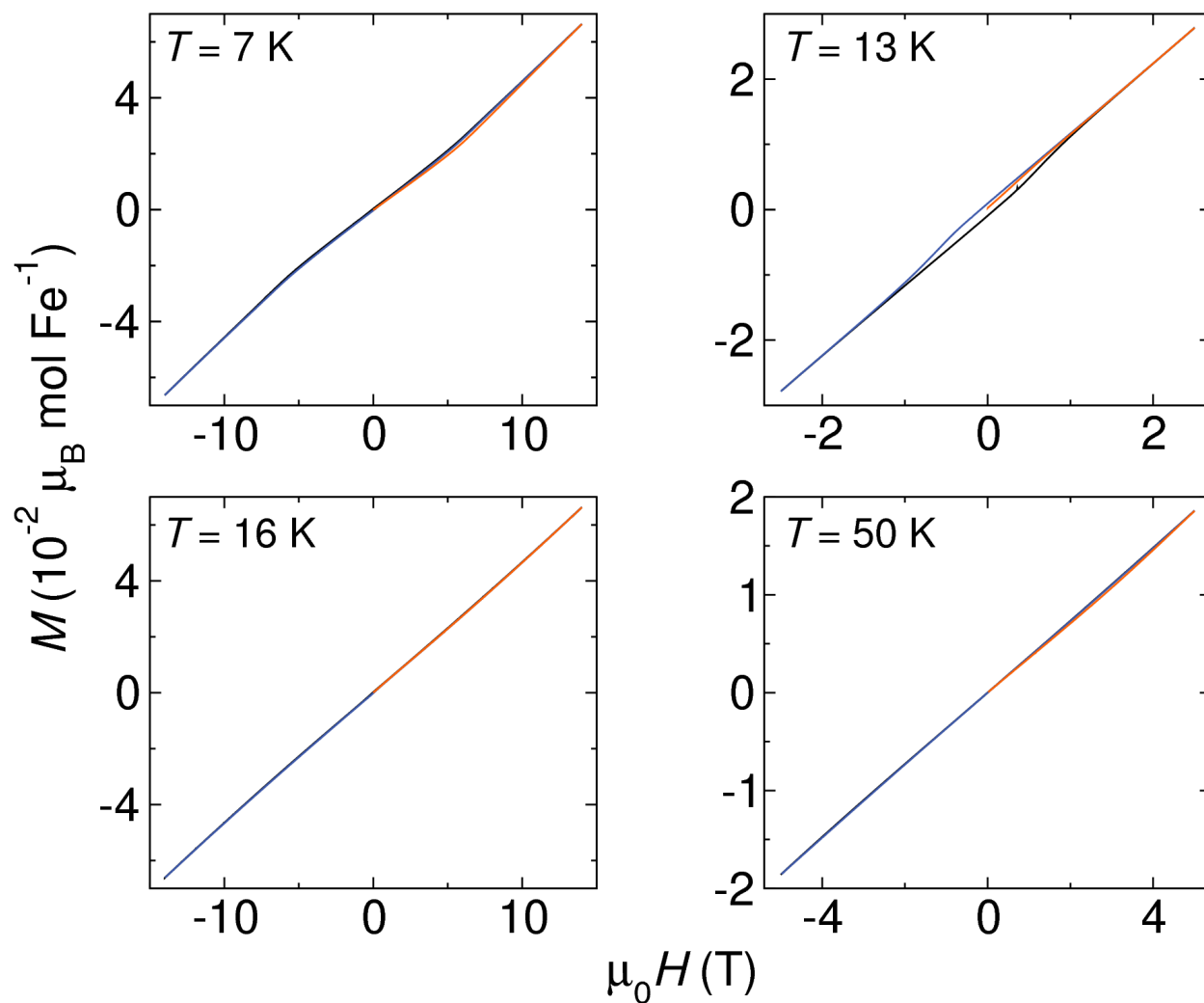
Figure A.4: Isothermal magnetization of fluorinated $Fe_3PO_4O_3$ at $T = 7, 13, 16, 50$ K. The virgin curve is shown in orange; at $T = 7, 50$ K the virgin curve lies outside the hysteresis loop, suggestive of a kinetically trapped magnetic state.